

The Inhomogeneous Background of H₂ Dissociating Radiation during Cosmic Reionization

Kyungjin Ahn¹, Paul R. Shapiro^{2,3}, Ilian T. Iliev^{4,5}, Garrelt Mellema⁶ and Ue-Li Pen⁷

¹ Department of Earth Science Education, Chosun University, Gwangju 501-759, Korea

E-mail: ¹ kjahn@chosun.ac.kr

² Department of Astronomy, University of Texas, Austin, TX 78712-1083, U.S.A

³ Texas Cosmology Center, the University of Texas at Austin, TX 78712, U.S.A

⁴ Universität Zürich, Institut für Theoretische Physik, Winterthurerstrasse 190, CH-8057 Zürich, Switzerland

⁵ Current address: Astronomy Centre, Department of Physics & Astronomy, University of Sussex, BRIGHTON BN1 9QH, England

⁶ Dept. of Astronomy, AlbaNova University Center, Stockholm University, SE 10691 Stockholm, Sweden

⁷ Canadian Institute for Theoretical Astrophysics, University of Toronto, 60 St. George Street, Toronto, ON M5S 3H8, Canada

Abstract. The first, self-consistent calculations are presented of the cosmological, H₂-dissociating UV background produced during the epoch of reionization by the sources of reionization. Large-scale radiative transfer simulations of reionization trace the impact of all the ionizing starlight on the IGM from all the sources in our simulation volume down to dwarf galaxies of mass $\sim 10^8 M_\odot$, identified by very high-resolution N-body simulations, including the self-regulating effect of IGM photoheating on dwarf galaxy formation. The UV continuum emitted below 13.6 eV by each source is then transferred through the same IGM, attenuated by atomic H Lyman series resonance lines, to predict the evolution of the inhomogeneous radiation background in the Lyman-Werner bands of H₂ between 11 and 13.6 eV. On average, the intensity of this Lyman-Werner background is found to rise to the threshold level at which dissociation suppresses H₂ cooling and star formation inside minihalos, long before reionization is complete. Spatial variations in the Lyman-Werner background are found which result from the clustering of sources associated with large-scale structure formation, such that intensity fluctuations correlate with matter density fluctuations. As a result, the Lyman-Werner background rises to the threshold level for H₂ suppression earlier in the vicinity of the reionization sources and their H II regions.

1. Introduction

Simulations suggest that the first stars in the Cold Dark Matter (“CDM”) universe formed inside minihalos of mass $M \sim 10^{5-6} M_\odot$ at $z \gtrsim 20$, when H₂ molecules cooled the primordial, metal-free halo gas and gravitational collapse ensued (e.g.

Bromm and Larson 2004 and references therein). This critical role of H₂ molecules as the primary coolants responsible for triggering the gravitational collapse that caused stars to form inside minihalos was limited, however, by the fact that H₂ can be dissociated by absorbing UV radiation in the H₂ Lyman-Werner (“LW”) bands in the energy range 11 – 13.6 eV. In the presence of a high enough LW-band radiation intensity, J_{LW} , the H₂ abundance would have been too low to cool the gas sufficiently to form stars. The threshold level of the intensity, $(J_{\text{LW}})_{\text{threshold}}$, above which minihalo star formation was suppressed is still uncertain. Early estimates (Haiman et al. 2000; henceforth, “HAR”) found that $(J_{\text{LW}})_{\text{threshold}}$ depended upon minihalo mass and redshift. In terms of the dimensionless quantity, $J_{\text{LW},21} \equiv J_{\text{LW}}/(10^{-21} \text{ erg s}^{-1} \text{ cm}^{-2} \text{ Hz}^{-1} \text{ sr}^{-1})$, they found that, to suppress H₂ for *all* minihalo masses, $(J_{\text{LW},21})_{\text{threshold}} \sim 10^{-2}$ to 1 was required, as redshift varied from $z \sim 10$ to 50, respectively. Later estimates, including those based upon 3D, numerical gas dynamical simulation of minihalos evolving in the presence of a LW background from more realistic cosmological initial conditions, found a similar range of threshold values (e.g. Ricotti et al. 2002; Yoshida et al. 2003; Yoshida et al. 2007).

Once stars began to form inside minihalos and also inside the rarer, more massive halos with $M \gtrsim 10^8 M_{\odot}$ virial temperatures above 10⁴K, in which radiative cooling by atomic hydrogen was possible even without H₂ (to cool the gas down to 10⁴K, at least, and initiate gravitational collapse), a rising diffuse LW background would have been inevitable, however. Starlight at energies below 13.6 eV, the ionization potential of atomic hydrogen, would have been largely free to escape from these star forming halos into the intergalactic medium (“IGM”), while the ionizing radiation above 13.6 eV was partially absorbed by the neutral hydrogen within the halos and thereby reduced by an escape fraction, f_{esc} . In that case, given the value of this f_{esc} and the ratio of the number of ionizing photons to the number of H₂-dissociating photons released by the stars, $N_{\text{i}}/N_{\text{LW}}$, which depends on the mass function and spectra of the stars, the rise of the cosmic LW background can, in principle, be related to the rise of the diffuse ionizing background. The latter is believed to have been responsible for the reionization of the intergalactic medium completed by redshift $z \gtrsim 6$. Estimates by HAR showed that the sources of this reionization would have caused the mean LW intensity in the IGM to exceed $(J_{\text{LW},21})_{\text{threshold}}$ long before reionization was complete.

This outcome is expected on quite general grounds, in fact. The mean number of LW photons in the background per H atom is related to the LW intensity according to:

$$\begin{aligned} \left(\frac{n_{\text{LW}}}{n_{\text{H}}}\right) &= \left(\frac{4\pi}{c} \int_{11.5 \text{ eV}}^{13.6 \text{ eV}} \frac{J_{\nu}}{h\nu} d\nu\right) / n_{\text{H}}, \\ &\simeq \frac{4\pi}{ch} \frac{2.1 \text{ eV}}{12.6 \text{ eV}} \langle J_{\nu} \rangle / n_{\text{H}}, \\ &\simeq 1.05 \times 10^{-5} J_{\text{LW},21} / n_{\text{H}}, \\ &\simeq 6.3 \times 10^{-3} J_{\text{LW},21} \left(\frac{1+z}{21}\right)^{-3}. \end{aligned} \quad (1)$$

Hence, if $(J_{\text{LW},21})_{\text{threshold}} < 1$, this implies that $(n_{\text{LW}}/n_{\text{H}})_{\text{threshold}} \lesssim 6 \times 10^{-3} (1+z)_{21}^{-3} \ll 1$.

The mean number of photons in the LW background per H atom at a given epoch is determined by their rate of emission per atom, integrated over time, reduced by a factor which accounts for attenuation and redshifting after emission. As discussed in § 2, photons emitted in the LW bands below 13.6 eV are removed from the background when they redshift to the frequency of the nearest H atom Lyman series transition from level $n \geq 3$ to $n = 1$. Only those sources within the distance from which photons emitted at the Ly γ frequency would be received at the Ly β frequency can contribute at all to the LW background at a given point. On average, roughly a third of the LW photons emitted within this horizon will survive their trip \ddagger . The same sources also emit UV photons with energies above 13.6 eV which are destroyed en-route by photoionizing H atoms. Reionization required that at least one ionizing photon was released into the IGM per H atom by the end of reionization. Let ξ_{LW} and ξ_{i} be the total number of LW and ionizing photons, respectively, released per H atom into the IGM up to some time. The mean number of photons per H atom in the LW background at that time is then roughly given by

$$\frac{n_{\text{LW}}}{n_{\text{H}}} \simeq \frac{1}{3} \left(\frac{\xi_{\text{LW}}}{\xi_{\text{i}}} \right) \xi_{\text{i}}. \quad (2)$$

For the stars believed to be responsible for reionization, the intrinsic ratio of ionizing UV photons to LW photons released, $N_{\text{i}}/N_{\text{LW}}$, ranged from $N_{\text{i}}/N_{\text{LW}} \sim 15$ (Pop III stars, high mass) to $N_{\text{i}}/N_{\text{LW}} \sim 1$ (Pop II stars, Salpeter IMF), while the escape fraction of ionizing photons was some $f_{\text{esc}} \ll 1$. In that case, we can write

$$\frac{n_{\text{LW}}}{n_{\text{H}}} \simeq \frac{1}{3} f_{\text{esc}}^{-1} \left(\frac{N_{\text{i}}}{N_{\text{LW}}} \right)^{-1} \xi_{\text{i}}, \quad (3)$$

and, therefore, if $(J_{\text{LW}, 21})_{\text{threshold}} < 1$, equations (1) and (3) imply that $(n_{\text{LW}}/n_{\text{H}})$ reaches the threshold level when ξ_{i} is only

$$(\xi_{\text{i}})_{\text{LW, threshold}} \simeq 3 \left(\frac{n_{\text{LW}}}{n_{\text{H}}} \right)_{\text{threshold}} \left(\frac{N_{\text{i}}}{N_{\text{LW}}} \right) f_{\text{esc}} \ll 1. \quad (4)$$

Accordingly, since reionization was not complete until the condition $\xi_{\text{i}} > 1$ was reached, the LW threshold for suppressing H₂ in the minihalos must have been reached long before the end of reionization. As a result, as HAR suggested, the minihalos were generally “sterilized” before they could contribute significantly to reionization.

What level of LW background is required to suppress minihalo star formation when the minihalos are also directly exposed to *ionizing* radiation, as well, is a more complicated question to answer. If a minihalo forms in a region of the IGM which is already photoionized, the pressure of the photoheated IGM there prevents it from collapsing gravitationally into the dark-matter dominated halo. Those minihalos are missing their baryonic component, therefore. This phenomenon, sometimes referred to as “Jeans-mass filtering” (Shapiro et al., 1994; Gnedin and Hui, 1998),

\ddagger This factor 1/3 comes from the survival rate from the attenuation by Lyman series resonance lines, given approximately by $\int_0^{r_{\text{LW}}} dr_{\text{os}} f_{\text{mod}}(r_{\text{os}}) / \int_0^{r_{\text{LW}}} dr_{\text{os}}$, where the terms used are described in § 2.2. Compare this expression to equation (29) and also see Figure 8.

ensures that H₂ cooling and star formation do not occur inside minihalos in the ionized regions of the IGM unless those minihalos had formed there *prior* to the arrival of the ionizing radiation. The impact of both LW *and* ionizing radiation (including X-rays) on *pre-existing* minihalos inside H II regions is a subject of ongoing work, beyond the scope of this paper (e.g. Machacek et al., 2001; Ricotti et al., 2002; Yoshida et al., 2003; Oh and Haiman, 2003; Shapiro et al., 2004; Iliev et al., 2005; Alvarez et al., 2006; Haiman and Bryan, 2006; Susa and Umemura, 2006; Mesinger et al., 2006; Ahn and Shapiro, 2007; Wise and Abel, 2007; Yoshida et al., 2007; O’Shea and Norman, 2008). The presence of dissociating radiation *always* implies the potential for limiting the H₂ abundance and, with it, the cooling required to make stars form. This is true even for the atomic-cooling halos above the minihalo mass range, although the level required for suppression might be higher. We shall focus here, however, on the rise of the LW background and its spatial variations contributed by the dominant sources of reionization, but leave the question of how the intensity impacts star formation for future studies.

Previous estimates of the cosmic LW background were limited to the *mean* background and were based upon a *homogeneous* approximation. These calculations assumed that the sources and the IGM were uniformly distributed, with uniform emissivity, given either by analytical approximation (HAR) or by summing over the sources found in small-box simulations, too small to account for the large-scale clustering of sources or to follow global reionization (e.g. Ricotti et al., 2002; Yoshida et al., 2003). Background of Ly α pumping radiation was considered semi-analytically by Barkana and Loeb (2005) and Pritchard and Furlanetto (2006), including the effects of fluctuations in the background in a linear approximation. The focus of these papers is on the Ly α intensity originating from photons that are absorbed by hydrogen Lyman resonance lines and converted into Ly α photons, which then radiatively mixes the 21 cm levels to drive the spin temperature to the gas kinetic temperature (Wouthuysen-Field effect), while we are interested in photons that remain unattenuated by Lyman resonance lines and affect H₂ abundance through photo-dissociation. Note that the horizon for sources responsible for the fluctuating Ly α background is considerably larger than that responsible for the LW background.

Here we present the first self-consistent radiative transfer calculations of the *inhomogeneous* LW background produced by the same sources which reionized the universe in a large-scale radiative transfer simulation of reionization. This problem presents a formidable computational challenge. The horizon for seeing LW photons is ~ 100 comoving Mpc, much larger than the size of typical H II regions (~ 10 Mpc). Since the mean free path for LW photons (~ 100 Mpc) is much larger than that for H-ionizing photons we must account for sources distributed over large volume and lookback time. Finally, the LW band photons are attenuated as they redshift into H-atom Lyman series resonance lines as they travel across the IGM. Hence, it is necessary to perform a multi-frequency radiative transfer calculation from each of the millions of sources in a cosmological volume larger than $\sim (100 \text{ Mpc})^3$, integrated along the light cones

from each source to every observation point they intersect, which is computationally prohibitive. As we shall show, a good approximation is possible which reduces the multi-frequency calculation to an equivalent gray opacity calculation. As a result, we are not only able to derive the evolution of the rising globally-averaged mean LW background during the epoch of reionization (EOR), but also to map its pattern of spatial variations over time. In § 2, we describe how continuum radiation emitted in the LW range below 13.6 eV is transferred through the IGM along the light cones from sources to observers, and how we solve this problem numerically. In § 3, we apply this method to one of our recent large-scale radiative transfer simulations of self-regulated reionization, described in Iliev, Mellema, Shapiro and Pen (2007). We compare the mean LW background evolution thus derived numerically with the homogeneous universe approximation and describe the spatial fluctuations of the LW background in some detail. Our conclusions are summarized in § 4. Some of our results on the inhomogeneous LW background during the EOR described here were first summarized in Ahn et al. (2008).

2. Radiative Transfer of the LW Background

2.1. Basic Equations

Let us first briefly describe how the inhomogeneous LW background can be calculated. Consider radiation sources distributed inhomogeneously. The mean intensity $J_\nu(\mathbf{x}_{\text{obs}}, z_{\text{obs}}, \nu_{\text{obs}})$ at observed frequency ν_{obs} at some comoving position \mathbf{x}_{obs} at redshift z_{obs} is given by

$$J_\nu(\mathbf{x}_{\text{obs}}, z_{\text{obs}}, \nu_{\text{obs}}) = \frac{1}{4\pi} \sum_s F_{\nu,s}(\mathbf{x}_{\text{obs}}, z_{\text{obs}}, \nu_{\text{obs}}), \quad (5)$$

where $F_{\nu,s}$ is the flux received at $(\mathbf{x}_{\text{obs}}, z_{\text{obs}}, \nu_{\text{obs}})$ that was emitted at $(\mathbf{x}_s, z_s, \nu_s)$ by a source (denoted by subscript s), where

$$\frac{\nu_s}{\nu_{\text{obs}}} = \frac{1 + z_s}{1 + z_{\text{obs}}}. \quad (6)$$

The position and redshift, (\mathbf{x}_s, z_s) , of a source are related to those of the observer at $(\mathbf{x}_{\text{obs}}, z_{\text{obs}})$ by the fact that the signal emitted at the epoch z_s must reach the position \mathbf{x}_{obs} at the epoch z_{obs} , travelling at the speed of light while the universe expands. We express this implicitly by writing the comoving separation, r_{os} , of the source and observer as follows:

$$r_{\text{os}} = |\mathbf{x}_{\text{obs}} - \mathbf{x}_s| = \int_{t(z_s)}^{t(z_{\text{obs}})} \frac{cdt}{a(t)} = - \int_{z_{\text{obs}}}^{z_s} c \frac{dz}{H(z)}. \quad (7)$$

If we specialize to the case of interest here ($z > 6$) in which the Hubble parameter $H(z)$ is given by the high-redshift limit for a flat universe with cosmological constant, equation (7) can be integrated to yield

$$\begin{aligned} r_{\text{os}} &= 2cH_0^{-1}\Omega_m^{-1/2}[(1 + z_{\text{obs}})^{-1/2} - (1 + z_s)^{-1/2}], \\ &= 2cH_0^{-1}\Omega_m^{-1/2}(1 + z_{\text{obs}})^{-1/2} \left[\left(\frac{\nu_{\text{obs}}}{\nu_s} \right)^{-1/2} - 1 \right], \end{aligned} \quad (8)$$

using equation (6).

The differential flux, $F_{\nu,s}$, received at $(\mathbf{x}_{\text{obs}}, z_{\text{obs}}, \nu_{\text{obs}})$ from a source of differential luminosity L_ν emitted at $(\mathbf{x}_s, z_s, \nu_s)$ is given by

$$F_{\nu,s}(\mathbf{x}_{\text{obs}}, z_{\text{obs}}, \nu_{\text{obs}}) = \frac{L_\nu(\nu = \nu_s)}{4\pi D_L^2(z_{\text{obs}}, z_s)} \cdot \left(\frac{1 + z_s}{1 + z_{\text{obs}}} \right) \cdot \exp[-\tau_{\nu_{\text{obs}}}], \quad (9)$$

where the factor $(1 + z_s)/(1 + z_{\text{obs}})$ reflects the fact that the observer sees the differential frequency interval reduced by redshift relative to the emitted interval. Here $D_L(z_{\text{obs}}, z_s)$ is the luminosity distance given by

$$D_L(z_{\text{obs}}, z_s) \equiv \left(\frac{r_{\text{os}}}{1 + z_{\text{obs}}} \right) \left(\frac{1 + z_s}{1 + z_{\text{obs}}} \right), \quad (10)$$

where the factor $(1 + z_s)/(1 + z_{\text{obs}})$ takes account of the redshifting of photon energies and arrival rates, which reduce the observed flux by $[(1 + z_{\text{obs}})/(1 + z_s)]^2$. The optical depth $\tau_{\nu_{\text{obs}}}$ depends on the observed frequency ν_{obs} according to

$$\tau_{\nu_{\text{obs}}} = \int_{t(z_s)}^{t(z_{\text{obs}})} \rho_b(\mathbf{x}, z) \kappa_{\nu'}(\mathbf{x}, z) c dt, \quad (11)$$

where $\nu' = \left(\frac{1+z}{1+z_{\text{obs}}} \right) \nu_{\text{obs}}$, $\rho_b(\mathbf{x}, z)$ is the baryon density at (\mathbf{x}, z) , $\kappa_{\nu'}(\mathbf{x}, z)$ is the opacity at (\mathbf{x}, z) to photons of frequency ν' , and where \mathbf{x} and z are the position and redshift of photons travelling along the line of sight which were emitted at (\mathbf{x}_s, z_s) and will be received at $(\mathbf{x}_{\text{obs}}, z_{\text{obs}})$.

The optical depth of the IGM to continuum UV photons in the LW range between 11.2 eV and 13.6 eV is predominantly due to resonant absorption by neutral H atoms in the Lyman series lines with upper states $n = i$, $i \geq 3$ (HAR). The mean optical depths in these lines can be written as follows:

$$\tau_i = \frac{f_{\text{osc},i} \nu_\alpha}{f_{\text{osc},\alpha} \nu_i} \tau_{\text{GP},\alpha} = \left(\frac{f_{\text{osc},i}}{0.416} \right) \left(\frac{0.75}{1 - 1/i^2} \right) \tau_{\text{GP},\alpha} \rightarrow 1.8 f_{\text{osc},i} \tau_{\text{GP},\alpha} \quad \text{for } i \gg 1, \quad (12)$$

where $f_{\text{osc},i}$ and $f_{\text{osc},\alpha}$ are the oscillator strengths and ν_i and ν_α are the frequencies, for lines of upper states $n = i$ and 2, respectively, and where $\tau_{\text{GP},\alpha}$ is the familiar Gunn-Peterson optical depth in the Lyman- α transition:

$$\begin{aligned} \tau_{\text{GP},\alpha} &= \left(\frac{\pi e^2}{m_e c} \right) \left(\frac{f_{\text{osc},\alpha}}{\nu_\alpha} \right) \left(\frac{c}{H(z)} \right) n_{\text{HI}} \\ &= 2.2 \times 10^6 \left(\frac{\Omega_b}{0.044} \right) \left(\frac{h}{0.7} \right)^{-1} \left(\frac{\Omega_m}{0.27} \right)^{-1/2} x_{\text{HI}} \left(\frac{1+z}{21} \right)^{3/2}, \quad (13) \end{aligned}$$

where n_{HI} is the mean number density of neutral hydrogen and x_{HI} is the mean neutral fraction of the IGM. Since we are most interested here in the early phases of the EOR, $x_{\text{HI}} = 1 - x_{\text{HII}} \approx 1$. As such, $\tau_{\text{GP},\alpha} \approx 10^6 \gg 1$. Even *inside* H II regions, however, $x_{\text{HI}} \gtrsim 10^{-4}$ (Iliev, Shapiro, McDonald, Mellema and Pen, 2007), so $\tau_{\text{GP},\alpha} \gg 1$ in general. As i increases, $f_{\text{osc},i}$ decreases (e.g. $f_{\text{osc},i} = 0.079, 0.029$, and 0.014 for $i = 3, 4$, and 5 , respectively (e.g. Höhne and Zimmermann, 1982), so there is some i_{max} such that $\tau_i < 1$ for $i > i_{\text{max}}$. For example, if *mean* IGM density is assumed in the ionized region with $x_{\text{HI}} \simeq 10^{-4}$, $i_{\text{max}} = 8, 7$, and 6 with $f_{\text{osc}} = 0.0032, 0.0048$, and 0.0078 at

$z = 20, 15,$ and $10,$ respectively. Note, however, that cosmic reionization occurs in an inside-out fashion, such that overdense regions are ionized earlier than the mean or underdense regions (e.g. Iliev, Mellema, Shapiro and Pen 2007). The effective i_{\max} in ionized regions, therefore, can be much larger than the estimates above. According to HAR, $i_{\max} \sim 150$ in the neutral IGM. It is a good approximation, therefore, to assume that the Lyman lines are optically thick for all i , since the frequency range over which the lines are not optically thick is a negligible fraction of the LW range below 13.6 eV.

The opacity of the IGM due to LW band absorption by H₂ is relatively unimportant by comparison, since the H₂ concentration in the IGM is small even before the LW background rises to suppress it. The pre-reionization H₂ concentration is $\sim 10^{-6}$ (Shapiro et al., 1994), and so $\tau_{\text{LW}} < 1$. We shall, henceforth, neglect this source of opacity. We refer the reader to §4 for more rigorous justification.

The expected number of computational operations required to evaluate equations (5) and (9) is $N_s \cdot N_g \cdot N_f$, where N_s is the number of sources, N_g is the number of grid cells on which J_ν is calculated, and N_f is the number of frequency-bins which are required to resolve the frequency dependence of $\tau_{\nu_{\text{obs}}}$ adequately. While these equations are straightforward, evaluating them numerically in a brute-force way can be prohibitively expensive in computational resources. For example, the H Lyman series resonance lines are optically thick to photons in the LW bands frequency range, and one should consider $N_f \gg 1$ to account for this effect properly. Currently, a full 3D, multi-frequency radiative transfer calculation is not feasible for the problem of interest. The effective number of sources N_s in our problem can be as large as 10^7 due to the large size of the LW horizon, and we need about $N_g \gtrsim 10^6$ grid-points to produce a statistically significant result. Cosmic reionization simulations, by contrast, do not require a multi-frequency operation, and yet, these simulations have only just become feasible recently with the help of massively-parallel computers.

The following sections describe how we overcome this technical difficulty in calculating the LW background by reducing N_f to 1, even though the net result becomes equivalent to a full multi-frequency radiative transfer calculation. We further describe in detail how we sum individual $F_{\nu,s}$'s, taking full account of the effect of redshifting and of the finite light-crossing time between sources and observers.

2.2. Attenuation of H₂ Dissociating Photons from a Single Source: the ‘‘Picket-Fence’’ Modulation Factor

For an inhomogeneous distribution of sources, we need to calculate the attenuation of continuum photons emitted in the LW energy range 11.2 - 13.6 eV separately for each individual source, by hydrogen Lyman line resonance absorption and subsequent cascades along the light cones from the source to every observer. Consider a source emitting continuum radiation at frequency ν_s at redshift $z = z_s$. As the photon travels toward the observer, it is absorbed when its frequency redshifts into an H Lyman series resonance line and, some of the time, the decay of the excited state replaces

the original photon with photons at frequencies below the range of the LW bands. If the original photon is resonantly scattered, it is quickly reabsorbed, until all resonant photons eventually turn into low-frequency photons below the LW bands. For this reason, Haiman et al. (1997, HRL, hereafter) and HAR assumed that, whenever the photons emitted in this range redshifted into one of the H Lyman resonance lines, they were completely attenuated and turned into low-frequency photons — mostly Ly α photons — out of the LW range. From the observer’s viewpoint, this leads to a series of “dark screens”, defined as sharp boundaries beyond which the observer cannot see any sources contributing LW intensity. These are marked by the maximum redshifts z_{\max} defined by

$$\frac{1 + z_{\max}}{1 + z_{\text{obs}}} = \frac{\nu_i}{\nu_{\text{obs}}}, \quad (14)$$

where ν_i is the frequency of the Lyman line closest to the observed frequency ν_{obs} from above. For a *homogeneous* universe with spatially-uniform emissivity, this results in the well-known “sawtooth” modulation of a uniform, isotropic LW background spectrum (HRL; HAR), an example of which we have plotted in Figure 1 for a homogeneous Λ CDM universe with flat-spectrum sources.

We shall make the same assumption here, that all LW photons are completely attenuated once they redshift into an H Lyman resonance line with upper state $n \geq 3$. However, we cannot limit ourselves to the homogeneous universe approximation. Since our objective is to consider contributions from individual sources that are distributed inhomogeneously, we must, instead, calculate how continuum photons emitted by *each* source will be attenuated by hydrogen atoms which they encounter along the particular line of sight that connects them with a given point of observation. We shall describe the attenuation of an individual source here in what follows. We shall then describe in § 2.3 how we sum over these individual source contributions to obtain the spatially-varying LW background intensity.

For the homogeneous universe in which the observed spectrum is transformed by the sawtooth modulation shown in Figure 1, this spectrum is the result of superposing the spectra of sources distributed continuously in lookback time along the line of sight. In that case, a given observed frequency combines the effect of photons emitted at different lookback times which experience different amounts of redshifting before reaching the observer. It is natural, then, to describe the modulation from the viewpoint of the observer, with the edge of each saw-tooth corresponding to the “dark screens” at the frequencies of the H Lyman lines, and the spectrum to the red side of a given line originating in the past from sources nearer than the distance to the corresponding screen. When we consider, instead, the spectrum of a single source in an inhomogeneous universe, there are also “dark screens” beyond which LW photons cannot pass, but these screens are best described from the point of view of the source. In that case, as a photon travels from the source, it will survive only until it encounters a “dark screen” in its future, as it redshifts into the nearest Lyman line. From the viewpoint of a source, the dark screens are located at the maximum radii that photons emitted at different

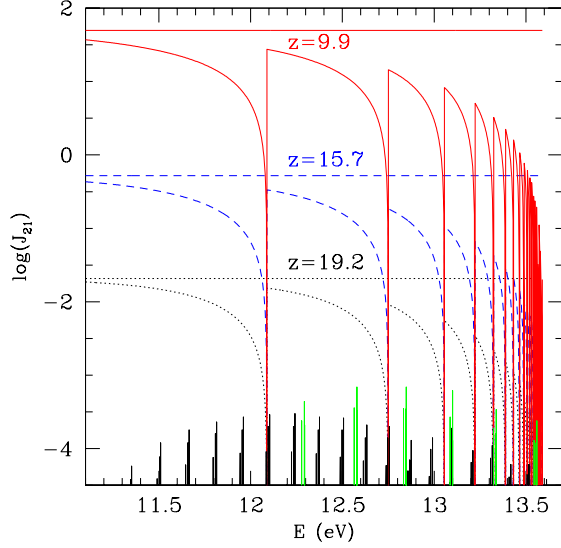


Figure 1. The observed “sawtooth” modulation of the uniform, isotropic radiation background observed in the UV range of the LW band range for a homogeneous Λ CDM universe with flat-spectrum sources, caused by H Lyman line opacity of the IGM (see text), for redshifts $z = 19.2$ (bottom lines, black), $z = 15.7$ (middle lines, blue) and $z = 9.9$ (top lines, red). The horizontal (dashed, corresponding colors) lines show the unattenuated mean intensity levels at these redshifts. A spatially uniform emissivity is assumed which evolves in time in proportion to the collapsed fraction of the matter density in halos massive enough to be sources of reionization, as described in § 3. Also plotted in vertical lines are the locations of relevant LW bands, when H₂ are assumed to be in the ground electronic state $X^1\Sigma_g^+$ with $v'' = 0$ and $J'' = 0, 1$. The height of these lines corresponds to $\log(0.01 \times f_{\text{osc}})$, where f_{osc} is the oscillator strength of Lyman (black) and Werner (green) bands compiled by Abgrall and Roueff (1989).

frequencies can travel from a source. Instead of equation (14), these radii are marked by minimum redshifts z_{min} defined by

$$\frac{1 + z_{\text{min}}}{1 + z_s} = \frac{\nu_i}{\nu_s}, \quad (15)$$

where ν_i is the (observed) frequency of the Lyman line closest to the emitted frequency ν_s from below. A screen corresponding to ν_i has the radius $r_i(\nu_s)$, where $r_i(\nu_s) \equiv r_{\text{os}}(\nu_i; \nu_s, z_s)$. This introduces finite frequency gaps in the transmitted spectrum, which as a consequence resembles a “picket fence”, with the intensity unattenuated between the dark gaps, as follows.

Consider a dark screen located at comoving distance $r_i(\nu_{i+1})$ from the source defined by

$$r_i(\nu_{i+1}) \equiv r_{\text{os}}(\nu_i; \nu_{i+1}, z_s), \quad (16)$$

where a photon emitted at ν_{i+1} from a source is redshifted into ν_i . At this location, all the photons with $\nu_s \geq \nu_i$ are completely attenuated in the following way. First, a

photon with $\nu_s = \nu_{i+1}$ will be redshifted into ν_i and attenuated at $r_i(\nu_{i+1})$ §. Any photons with ν_s in between ν_i and ν_{i+1} will then be redshifted into ν_i and attenuated at some distance shorter than $r_i(\nu_{i+1})$. Since no photon can cross a Lyman line frequency as it is redshifted, the observed spectrum will be completely black inside a trough between ν_i and ν_{i+1} . For $\nu_{i+1} \leq \nu_{\text{obs}} < \nu_{i+2}$, this will happen at $r_{i+1}(\nu_{i+2})$. Because

$$r_{i+1}(\nu_{i+2}) < r_i(\nu_{i+1}), \quad (17)$$

the observed spectrum at $r_i(\nu_{i+1})$ will also have a trough from ν_{i+1} to ν_{i+2} . This way, all the photons with $\nu_{\text{obs}} \geq \nu_i$ are completely attenuated at $r_{\text{os}} = r_i(\nu_{i+1})$. On the other hand, because $r_{i-1}(\nu_i) > r_i(\nu_{i+1})$, a photon with $\nu_s = \nu_i$ has not fully redshifted into ν_{i-1} but only into $\nu_{\text{obs}}(r_i(\nu_{i+1}); \nu_i, z_s)$ at $r_i(\nu_{i+1})$, where

$$\nu_{\text{obs}}(r_{\text{os}}; \nu_s, z_s) \equiv \nu_s \left[1 + \frac{H_0 \Omega_m^{1/2}}{2c} (1 + z_s)^{1/2} r_{\text{os}} \right]^{-2}, \quad (18)$$

obtained from equation (8). Photons with the observed frequency ranging from ν_{i-1} to $\nu_{\text{obs}}(r_i(\nu_{i+1}); \nu_i, z_s)$ will have reached $r_i(\nu_{i+1})$ without attenuation. Therefore, the spectrum will have full transmission for $\nu_{i-1} < \nu_{\text{obs}} < \nu_{\text{obs}}(r_i(\nu_{i+1}); \nu_i, z_s)$, while there is a completely black trough for $\nu_{\text{obs}}(r_i(\nu_{i+1}); \nu_i, z_s) \leq \nu_{\text{obs}} < \nu_i$. Similarly, the next lower-energy interval, defined by $\nu_{i-2} < \nu_{\text{obs}} < \nu_{i-1}$, will have full transmission for $\nu_{i-2} < \nu_{\text{obs}} < \nu_{\text{obs}}(r_i(\nu_{i+1}); \nu_{i-1}, z_s)$ and a trough for $\nu_{\text{obs}}(r_i(\nu_{i+1}); \nu_{i-1}, z_s) \leq \nu_{\text{obs}} < \nu_{i-1}$. As a result, the observed relative flux is affected by what we call the ‘‘picket-fence’’ modulation, as depicted in Figure 2.

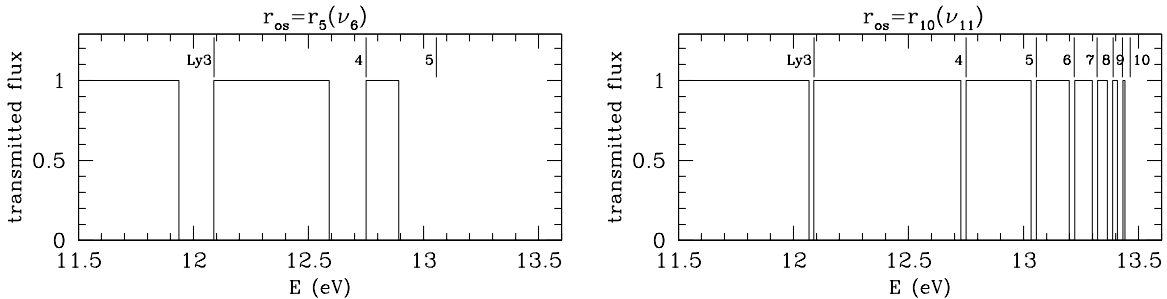


Figure 2. Transmitted spectrum from a single source: picket-fence modulation. (*left*) Relative flux observed at $r_5(\nu_6)$, where a photon emitted at Ly5 (Ly ϵ) frequency is redshifted into Ly4 (Ly δ) frequency. (*right*) Relative flux observed at $r_{10}(\nu_{11})$, where a photon emitted at Ly11 frequency is redshifted into Ly10 frequency. We use a convention that the energy of Ly i photon is $13.6 \text{ eV} (1 - 1/i^2)$. The location of several Lyman resonance lines Ly i is shown in vertical lines and denoted by i in both panels.

Note that, at a fixed distance, $\nu_{\text{obs}} \propto \nu_s$ from equation (18). A gap appearing between observed frequencies ν_j and ν_{j+1} at some r_{os} is also proportional to ν_{j+1} . If we

§ A more accurate description is that a photon with frequency slightly smaller than ν_{i+1} is redshifted into ν_i and attenuated at distance slightly shorter than $r_i(\nu_{i+1})$, because a photon with $\nu_s = \nu_{i+1}$ is attenuated on-site right after being emitted. However, we give the description in the text for simplicity.

call the size of this gap $\Delta\nu_{\text{gap},j+1}$, we then have

$$\frac{\Delta\nu_{\text{gap},j+1}}{\Delta\nu_{\text{gap},i+1}} = \frac{\nu_{j+1}}{\nu_{i+1}}, \quad (19)$$

as long as the range of frequency, $[\nu_j, \nu_{j+1}]$, is not fully covered by $\Delta\nu_{\text{gap},j+1}$.

We define the picket-fence modulation factor f_{mod} by

$$f_{\text{mod}}(r_{\text{os}}; z_{\text{s}}) \equiv \langle \exp(-\tau_{\nu_{\text{obs}}}) \rangle \equiv \frac{\int_{11.5 \text{ eV}}^{13.6 \text{ eV}} d(h\nu_{\text{obs}}) \exp(-\tau_{\nu_{\text{obs}}})}{\int_{11.5 \text{ eV}}^{13.6 \text{ eV}} d(h\nu_{\text{obs}})}, \quad (20)$$

which is a function only of the comoving distance r_{os} and the source redshift z_{s} . We choose 11.5 eV as the minimum energy of interest, because the dissociation rate for the LW bands at $h\nu < 11.5 \text{ eV}$ is negligible compared to that for those at $h\nu > 11.5 \text{ eV}$ (see, e.g., Figure 1 of HAR). When H₂ molecules absorb photons in the LW bands, in general only about 15% of these excitations lead to dissociation of H₂. When a single source is observed at some comoving distance r_{os} , some LW bands will be excited by fully transmitted photons, which results in dissociation about 15% of the time, therefore, while other bands will not, because they reside in a trough. For sources of interest here, we can approximate L_{ν} by a flat spectrum whose amplitude is given by the frequency-averaged luminosity $\langle L_{\nu} \rangle \equiv \int_{11.5 \text{ eV}}^{13.6 \text{ eV}} d(h\nu_{\text{s}}) L_{\nu}(\nu_{\text{s}})/(2.1 \text{ eV})$. This is a fairly good approximation, unless the spectrum is unusually steep in the narrow energy range of interest, [11.5 – 13.6] eV. For example, both black-body spectra with $T = [5 - 10] \times 10^4 \text{ K}$ and a power-law spectrum with $L_{\nu} \propto \nu^{-1}$ have a maximum deviation from $\langle L_{\nu} \rangle$ which is smaller than 10% in this energy range. In that case, because the LW bands are almost uniformly distributed in frequency, the true dissociation rate will be almost identical to that obtained by assuming that all the H₂ LW lines experience the frequency-averaged value of the LW intensity after the picket-fence modulation. Therefore, in addition to the geometrical dilution of the incident flux, the H₂ dissociation rate will be suppressed in proportion to f_{mod} . This f_{mod} is just the fraction of the total frequency interval from 11.5 to 13.6 eV observed at z_{obs} from a source at z_{s} at comoving distance r_{os} occupied by the full transmission windows in between the dark troughs, as described above. Hence,

$$f_{\text{mod}} = 1 - \sum_j \left(\frac{h\Delta\nu_{\text{gap},j}}{2.1 \text{ eV}} \right). \quad (21)$$

The picket-fence modulation factor is a key ingredient in alleviating computational difficulties which would have arisen due to a multi-frequency calculation. We have calculated f_{mod} numerically and found a simple fitting formula which fits the true values within a 2% error (see Figure 3):

$$f_{\text{mod}} = \begin{cases} 1.7 \exp[-(r_{\text{cMpc}}/116.29\alpha)^{0.68}] - 0.7 & \text{if } r_{\text{cMpc}}/\alpha \leq 97.39 \\ 0 & \text{if } r_{\text{cMpc}}/\alpha > 97.39 \end{cases} \quad (22)$$

where r_{cMpc} is r_{os} in units of comoving Mpc, and α is a scaling factor given by

$$\alpha = \left(\frac{h}{0.7} \right)^{-1} \left(\frac{\Omega_m}{0.27} \right)^{-1/2} \left(\frac{1+z_{\text{s}}}{21} \right)^{-1/2}. \quad (23)$$

We call $r_3(\nu_4)$, which is equal to 97.39α cMpc, the “LW horizon” r_{LW} . This is the maximum comoving distance from a source that an H₂ dissociating photon can reach, corresponding to the distance from which the redshift produces the maximum frequency difference possible between two adjacent lines in the Lyman series (as long as we restrict the observed energy range to [11.5 - 13.6] eV). Note that all the dark screen distances are scaled by α , which increases as z_s decreases.

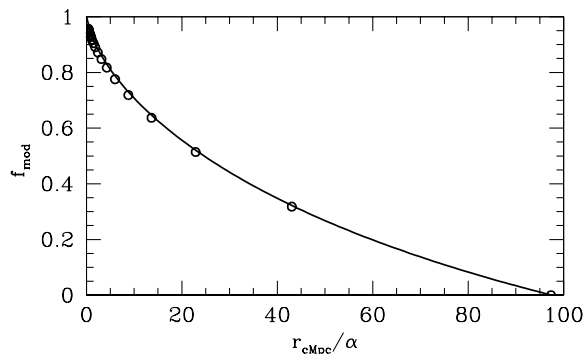


Figure 3. Picket-fence modulation factor f_{mod} as a function of comoving distance r_{cMpc} in units of Mpc. True values at selected radii $r_i(\nu_{i+1})$ (open circle) and a fit (solid curve) are plotted. α , given by equation (23), is a distance scaling factor which depends on redshift. When $r_{\text{cMpc}} = 97.39\alpha$, $f_{\text{mod}} = 0$, which sets the “LW horizon” for H₂ dissociating radiation from a source.

2.3. Intensity of H₂ dissociating photons from multiple sources

The path of a photon in the expanding universe follows a null geodesic. The Friedmann-Robertson-Walker metric for a homogeneous, isotropic universe is given by

$$ds^2 = dt^2 - a^2(t) [dr^2 + r^2 d\Omega^2] = a^2(t) [d\tau^2 - (dr^2 + r^2 d\Omega^2)], \quad (24)$$

where we adopt natural units with $c = 1$. In that case, the comoving distance travelled by a photon since its emission is given by setting $ds^2 = 0$ in equation (24), solving for dr ($d\Omega = 0$), and integrating over time to yield the conformal time τ , defined by

$$\tau = \int d\tau = \int dt/a(t). \quad (25)$$

We use this fact to construct the world lines of sources and their radiation, shown in Figure 4. If our choice of space-time coordinates is the comoving distance and the conformal time, then null geodesics make straight lines at a 45° angle. World lines of the sources, on the other hand, will be close to straight lines, parallel to the conformal time axis. For simplicity, we will neglect the small peculiar motion of halos.

We must account for the finite light-crossing time for light from sources to reach an observer, because these are distributed over a truly cosmological volume and the population of sources can vary significantly over the lookback time corresponding to $r_{\text{LW}} \sim 100$ cMpc, due to the rapid evolution of cosmological structure. The conformal

space-time diagram of sources mentioned above becomes a useful tool for this task. At a given redshift we draw past light cones from an observing point, which have a maximum length equal to the LW horizon length, r_{LW} . When the world line of a source intersects one of these past light cones, we add its flux contribution to the mean intensity at the corresponding observing point (see Figure 4). The fact that $\Delta\tau = r_{\text{os}}$, where $\Delta\tau$ is the conformal lookback time to a source at comoving distance r_{os} from the observing point, makes it easy to find these intersecting points as well as the source redshift. The conformal time interval, τ_{LW} , which corresponds to the LW horizon, r_{LW} , determines how far back in look-back time a given observer cell at a given epoch z_{obs} must extend its past light-cone to look for contributing sources. Accordingly, this operation requires that the past light-cones extend back through a number, n_{steps} , of time steps, Δt , equal to $\tau_{\text{LW}}/\Delta t$.

After a contributing source is found, its frequency-averaged LW flux observed at the given \mathbf{x}_{obs} and z_{obs} is evaluated using equation (9), replacing L_ν by its average over the LW band frequency and replacing $\exp(-\tau_{\text{obs}})$ by f_{mod} using equations (22) and (23). We sum fluxes from all the sources (denoted by the subscript s) observed within the LW horizon.

3. The Inhomogeneous LW Background from a Simulation of Cosmic Reionization

3.1. Illustrative Case: Self-Regulated Reionization

As an example, we apply the methodology for calculating the fluctuating LW background described in the previous sections to one of our large-scale N-body and radiative transfer simulations of cosmic reionization presented in Iliev, Mellema, Shapiro and Pen (2007, henceforth “IMSP”). The cosmological structure formation and evolution is followed with a particle-mesh N-body code called PMFAST (Merz et al. 2005). These N-body results then provide the evolving density field of the IGM (coarsened to a lower resolution than the original particle-mesh grid in order to make the radiative transfer feasible) and the location and mass of all the halo sources, as input to a separate radiative transfer simulation of inhomogeneous reionization. The latter simulation is performed by our C²-Ray (Conservative, Causal Ray-Tracing) code, a grid-based, ray-tracing, radiative transfer and nonequilibrium chemistry code, described in Mellema et al. (2006). The ionizing radiation is ray-traced from every source to every grid cell at a given timestep using a method of short characteristics. The code is explicitly photon-conserving in both space and time, which ensures an accurate tracking of ionization fronts, independent of the spatial and time resolution, even for grid cells which are optically thick to ionizing photons and time steps long compared to the ionization time of the atoms, with correspondingly great gains in efficiency. The code has been tested against analytical solutions (Mellema et al. 2006) and, in direct comparison with other radiative transfer methods, on a standardized set of benchmark problems

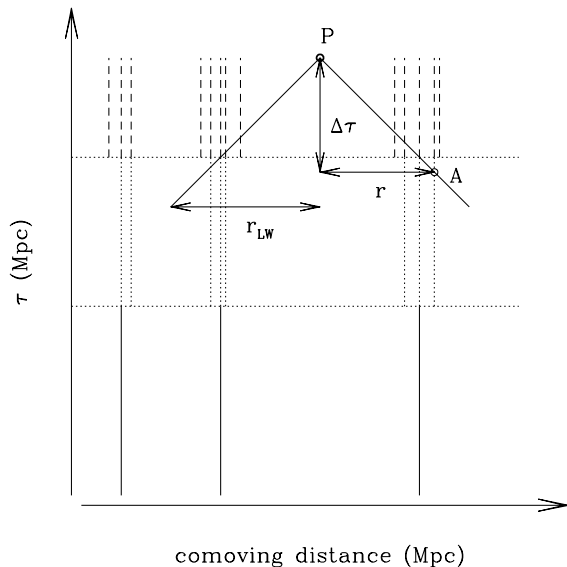


Figure 4. Conformal space-time diagram of radiation sources and the past light cone of an observer, used to identify which of the sources in the N-body simulation volume in the past emitted light just now reaching the observer at a given time. Radiation sources are created discretely in time in the N-body simulation results — i.e. source catalogue is constructed at each output time (dotted horizontal lines). The location of each source is assumed to stay constant during each time step (shown as solid, dotted, and short-dashed vertical lines) as are the source luminosities. Photons follow null geodesics truncated at the LW horizon r_{LW} , and an observer at point P will see sources whose world lines intersect with the past light-cone. The flux contributed by these sources are determined by where these intersecting points lie along the time axis. We use a coordinate system composed of comoving distance and conformal time, for computational ease. For example, the conformal lookback time $\Delta\tau$ (Mpc) from point P to a source at point A, which determines the emitting redshift and the source flux, is easily obtained once the comoving distance r (Mpc) to the source is known, because $\Delta\tau = r$.

(Iliev, Ciardi, Alvarez, Maselli, Ferrara, Gnedin, Mellema, Nakamoto, Norman, Razoumov, Rijkhorst, Rit, 2006).

We simulated the Λ CDM universe with 1624^3 dark matter particles of mass $10^6 M_\odot$, in a comoving simulation volume of $(35 h^{-1} \text{ Mpc})^3$. This allowed us to resolve (with 100 particles or more per halo) all halos with mass of $10^8 M_\odot$ or above. This is roughly the minimum mass of halos which can radiatively cool by hydrogen atomic-line excitation and efficiently form stars. The radiative transfer grid has 203^3 cells.

The H-ionizing photon luminosities per halo in our cosmic reionization simulations are assigned in the following way. Halo catalogues are discrete in time, because N-body density fields are stored every ~ 20 Myrs and the corresponding source (halo) catalogues are produced at the same time. A halo of mass M is assumed to have converted a mass $M \cdot (\Omega_b / \Omega_m) \cdot f_*$ into stars, where f_* is the star formation efficiency^{||}. If each source forms

^{||} Not all the halos convert their mass into stars. Halos inside H II regions are assumed to be “failed”

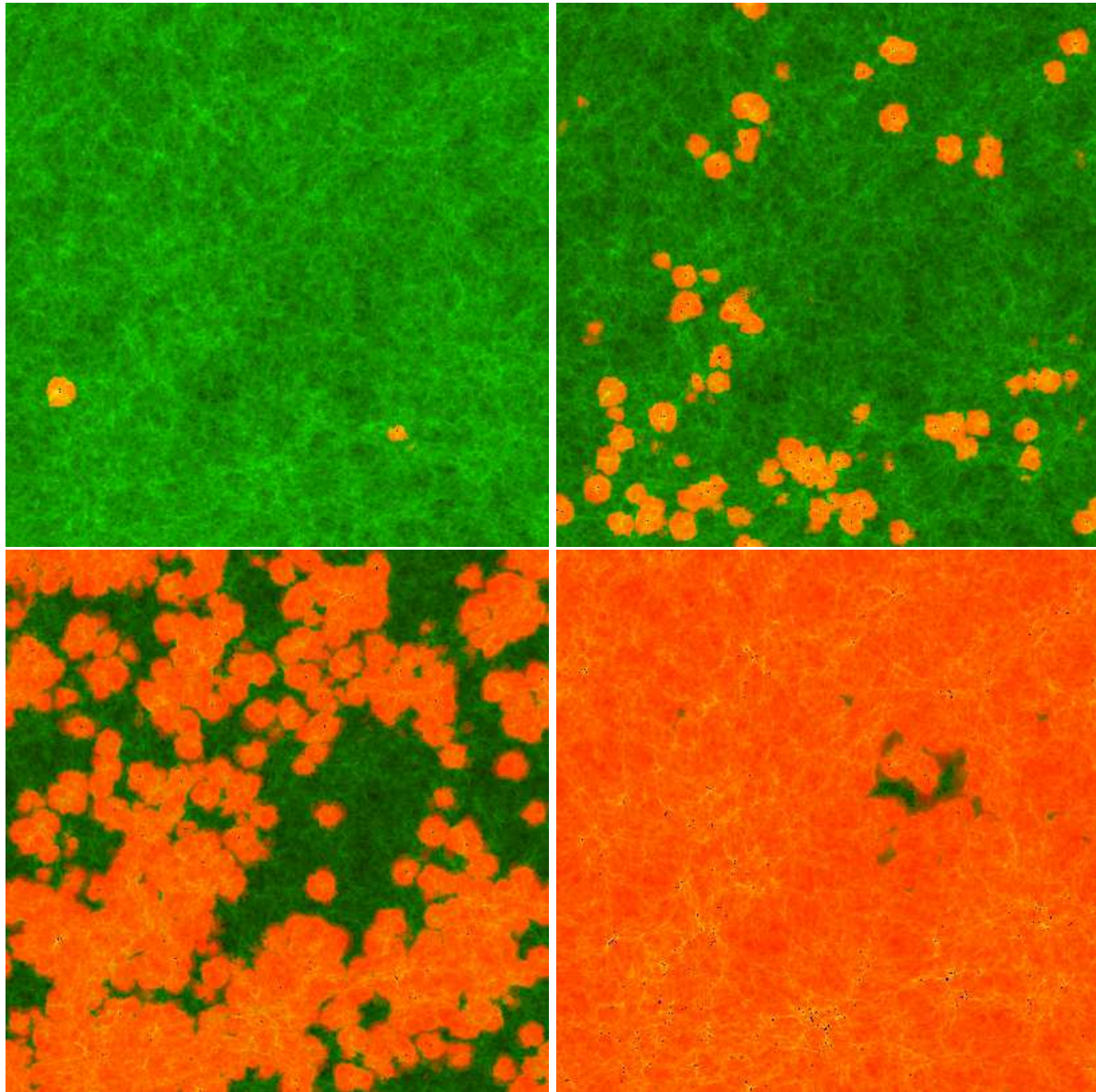


Figure 5. Spatial slices of the ionized and neutral gas density from self-regulated simulation (IMSP; f2000.250S case), at redshifts $z = 15.7$ (top-left), 12.9 (top-right), 9.9 (bottom-left), and 7.9 (bottom-right). The volume-weighted (mass-weighted) global ionized fractions at these redshifts are 6.4×10^{-3} (9.7×10^{-3}), 0.12 (0.15), 0.56 (0.62), and 0.99 (0.99), respectively. Shown are the density field (green) overlaid with the ionized fraction (red/orange), and cells containing active sources are shown as dots. Each slice has a thickness of $86 h^{-1} \text{ckpc}$, while sources shown are from a thicker ($\sim 1.8 h^{-1} \text{cMpc}$) region.

stars over a period of time Δt and each stellar baryon produces N_i ionizing photons per sources (i.e. their ability to form stars is suppressed by the photoionization which created the H II region) if their mass is below $10^9 M_\odot$. More realistically, source formation in halos of this mass range may have a gradual dependence on halo mass: as mass decreases, it is harder to form sources inside, and vice versa (Mesinger and Dijkstra, 2008). Nevertheless, as halo population is dominated by lowest-mass halos, which are most vulnerable to photoheating in this mass range, we adopt our

stellar lifetime and is used only once per Δt , and if a fraction f_{esc} of these photons escape into the IGM, the ionizing photon number luminosity of a halo of mass M will be given by

$$Q_i = \frac{N_i \cdot f_{\text{esc}} \cdot f_* \cdot M (\Omega_b / \Omega_m)}{\Delta t \cdot \mu m_H}, \quad (26)$$

where μ is the mean molecular weight and m_H is the mass of a hydrogen atom. In this model, stars are produced in a burst, and they keep radiating with fixed Q_i for $\Delta t \simeq 20$ Myrs. It is noteworthy that the result does not depend on the detailed shape of the source spectrum, but only on a frequency-integrated parameter N_i .

We calculate $\langle L_\nu \rangle$ for the LW background sources in a similar way. All H-ionizing sources also produce H₂ dissociating photons, and their $\langle L_\nu \rangle$ is also constant during the source lifetime Δt . In each succeeding time interval, Δt , new sources are identified with the halo catalogue for that time-slice in the N-body results and are assumed to emit radiation with constant $\langle L_\nu \rangle$. This $\langle L_\nu \rangle$ is proportional to $(Q_i / f_{\text{esc}})(N_{\text{LW}} / N_i)$, where the proportionality constant is the dimensional factor which indicates the frequency-integrated number of ergs s⁻¹ Hz⁻¹ per LW photon released in the source spectrum. We then construct the future world lines of these sources across the source lifetimes, Δt . At a given observing redshift, we then draw past light cones from every grid point in the simulation box. When the past light cone of an observer intersects the world line of a certain source, we register the comoving distance r_{os} to that source and its flux contribution.

We choose here a specific case from IMSP, the self-regulated reionization case “f2000_250S” with *WMAP3* background cosmology. In this scenario, small-mass halos ($10^8 \lesssim M/M_\odot \lesssim 10^9$) host high-efficiency emitters with top-heavy initial mass function, or “IMF” (e.g. massive Pop III stars). The (hydrogen-ionizing) photon production efficiency, $f_\gamma \equiv f_* f_{\text{esc}} N_i$, of these sources is approximated by $f_\gamma = 2000$. On the other hand, large-mass halos ($M/M_\odot \gtrsim 10^9$) are assumed to host lower-efficiency emitters approximated by $f_\gamma = 250$ (e.g. Pop II stars with Salpeter IMF). The simulation box has a volume $(35 h^{-1} \text{Mpc})^3$, with $h = 0.73$. The reader is referred to IMSP for more details.

At this point, we need to deal with the fact that the simulation box ($35 h^{-1} \text{cMpc}$ in this case) is smaller than the LW horizon ($97.39\alpha \text{cMpc}$). We simply use a periodic box condition, attaching identical boxes around the domain of calculation. We use 5^3 identical boxes in total, choosing the central one as the domain of computation. One may, instead, shift and rotate boxes before attaching them: however, this approach would not be able to remove the finite-box effect completely either. In the future, we will use a much larger simulation box, which will naturally reduce this effect.

We parallelized our code using the message passing interface library (MPI) to calculate the evolution of the spatially-varying LW background on distributed-memory parallel computers. We used “Lonestar”, a massively-parallel supercomputer at the simple prescription in this paper.

Texas Advanced Computing Center (TACC) at the University of Texas at Austin. It has a total of 5,200 cores of dual-core Intel Xeon 5100 processors and 11.6 TB of aggregate memory. The particular run of LW background calculation presented here – run separately from the cosmic reionization simulation – took about 15 hours of computing time on Lonestar, when we used 256 computing cores and about 1.5 GB memory per core. The numbers of halos on the radiative transfer grid of 203^3 cells in the simulation box of $35 h^{-1}$ cMpc were about 1.3×10^3 , 7×10^4 , and 1.9×10^5 at $z \simeq 15$, 10, and 8, respectively. Note that the effective total number of sources for our LW background calculation is about 125 times the number of sources in the simulation box of this particular size, due to the length scale of r_{LW} .

3.2. Evolution of the Globally-Averaged Ionizing and Dissociating Radiation Backgrounds

The growth and geometry of the ionized fraction of the universe during the EOR is illustrated by the selected time-slices shown in Figure 5. The corresponding evolution of the globally-averaged ionized fraction and the ionizing and dissociating radiation backgrounds is summarized in Figure 6, with several interesting features revealed. First, at $z \gtrsim 10$, small-mass halos dominate the large-mass halos in contributing both ionizing and dissociating photons. This is easily understood in the framework of the standard Λ CDM cosmology, because the population of low-mass halos dominates over that of high-mass halos, both in numbers and in total mass. These low-mass sources, however, become “self-regulated” as the universe gets more ionized (since they are suppressed as sources in the H II regions) and are later almost fully suppressed at $z \lesssim 10$, while the collapsed fraction in the unsuppressible (higher-mass) sources only grows with time. Thus, both reionization and dissociation are dominated by high-mass halos at $z \lesssim 10$. Second, n_i/n_{LW} becomes smaller at $z \lesssim 10$ than at $z \gtrsim 10$. This is simply due to the transition of major source type from Pop III to Pop II, because $(N_i/N_{\text{LW}})_{\text{III}} > (N_i/N_{\text{LW}})_{\text{II}}$.

We note that the reionization history depends on the adopted values of the efficiency parameters, f_γ , for low-mass and high-mass halos. The ionizing background is degenerate in f_* , f_{esc} and N_i , in fact, as long as their product f_γ is fixed. This is not true for the dissociating background, however, which breaks the degeneracy between f_{esc} and N_i , in general. Because dissociating photons — with emitted energy ranging from 11.2 eV to 13.6 eV — are largely unattenuated by their own interstellar medium inside the source halos, their escape fraction from the source halo is essentially unity. Therefore, for a given f_γ , or a given reionization history,

$$J_{\text{LW},21} \propto 1/f_{\text{esc}}.$$

Hardness of the spectral energy distribution (SED) of the source, which can be characterized by N_i/N_{LW} , also affects $J_{\text{LW},21}$. For a given f_γ ,

$$J_{\text{LW},21} \propto (N_i/N_{\text{LW}})^{-1}.$$

Assuming a top-heavy IMF, Pop III objects have $(N_i/N_{\text{LW}})_{\text{III}} \approx 15$ (e.g. Tumlinson and Shull, 2000; Bromm et al., 2001). Pop II objects with a Salpeter IMF, on the other hand, have $(N_i/N_{\text{LW}})_{\text{II}} \approx 1$ (Tumlinson and Shull 2000 and references therein).

The spatially-averaged mean intensity is already as high as $\langle J_{\text{LW},21} \rangle = 0.1$ by $z \approx 15$, when the mean ionized fraction of the universe is only $\langle x \rangle \approx 0.02$, if the fiducial value of $f_{\text{esc,III}} = 0.2$ is used for Pop III objects. $J_{\text{LW},21}$ is not affected by $f_{\text{esc,II}}$ until $z \approx 15$, because Pop II objects start to emerge only after $z \approx 15$. As described above, $J_{\text{LW},21}$ is proportional to $1/f_{\text{esc}}$. For instance, if $f_{\text{esc,III}} = 1$ instead of 0.2, then $\langle J_{\text{LW},21} \rangle = 0.1$ will be reached later after $z \approx 15$. $\langle J_{\text{LW},21} \rangle$ depends on both $f_{\text{esc,III}}$ and $f_{\text{esc,II}}$ at $z \lesssim 15$, and if $f_{\text{esc,II}}=1$ as well, then $\langle J_{\text{LW},21} \rangle = 0.1$ at $z \approx 13$, or when $\langle x \rangle \approx 0.1$.

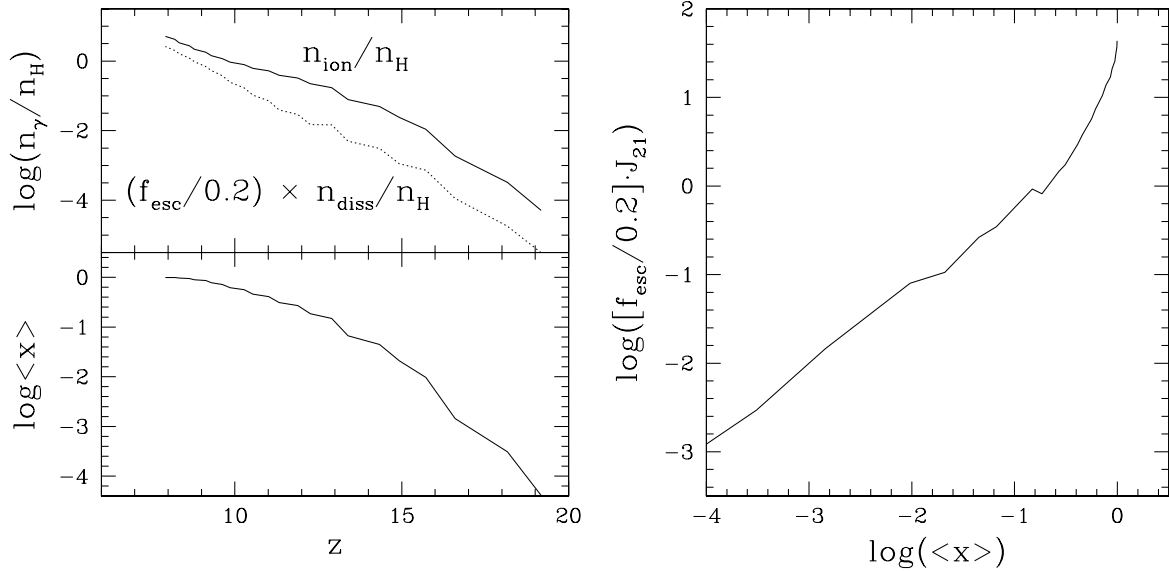


Figure 6. Global history of cosmic reionization and the dissociation background: (Left panel)(top) Evolution of the photon to baryon ratios, where n_{ion} is the total ionizing photon number density accumulated until given redshift z , while n_{LW} is the “instantaneous” dissociating photon number density at z given by $n_{\text{LW}} \equiv \frac{4\pi}{c} \int_{11.5 \text{ eV}}^{13.6 \text{ eV}} \frac{J_\nu}{h\nu} d\nu \simeq \frac{4\pi}{ch} \frac{2.1 \text{ eV}}{12.6 \text{ eV}} \langle J_\nu \rangle$. (bottom): Global mean ionized fraction $\langle x \rangle$ vs. redshift. (Right panel): Global mean dissociating intensity, $\langle J_{\text{LW},21} \rangle$, multiplied by $(f_{\text{esc}}/0.2)$, vs. the global mean ionized fraction.

It is useful to compare our numerical results for the space-averaged LW intensity with the homogeneous universe approximation. The global mean dissociating intensity $\langle J_{\text{LW},21} \rangle$ is easily predictable if the fraction of mass collapsed into stars and the number of dissociating photons created per stellar baryon are known. Consider a universe where sources are homogeneously distributed, with a collapsed fraction which is identical to that obtained numerically from our N-body simulation. The emission coefficient (in

erg s⁻¹ Hz⁻¹ sr⁻¹ cm⁻³) is then only a function of redshift as follows:

$$j_{\nu_s}(z_s) = \frac{1}{4\pi} \epsilon_{\nu_s} \rho_m(z_s) \frac{\Omega_b}{\Omega_m} f_{\text{coll}}(z_s) f_*, \quad (27)$$

where ϵ_{ν_s} (erg s⁻¹ Hz⁻¹ g⁻¹) is the emissivity at emitted frequency ν_s , $\rho_m(z_s)$ is the mean mass density at redshift z_s , and $f_{\text{coll}}(z_s)$ is the source halo collapsed fraction. Note that this is the proper emission coefficient: the comoving emission coefficient is given by

$$\begin{aligned} \bar{j}_{\nu_s}(z_s) &\equiv j_{\nu_s}(z_s)/(1+z_s)^3 \\ &= \frac{1}{4\pi} \epsilon_{\nu_s} \rho_{m,0} \frac{\Omega_b}{\Omega_m} f_{\text{coll}}(z_s), \end{aligned} \quad (28)$$

where $\rho_{m,0}$ is the mean mass density at present. Finally, the (proper) mean intensity in this homogeneous universe is obtained by

$$\langle J_\nu \rangle_{\text{homo}}(z_{\text{obs}}) = (1+z_{\text{obs}})^3 \int_0^{r_{\text{LW}}} \frac{dr_{\text{os}}}{1+z_s} \bar{j}_{\nu_s}(z_s) \cdot f_{\text{mod}}(r_{\text{os}}), \quad (29)$$

where the source redshift z_s is implicitly related to r_{os} by equation (8). The emission coefficient $\bar{j}_{\nu_s}(z_s)$ is shown in Figure 7, where the “stair-steps” reflect the fact that, as described in § 2.3, we use halo catalogues that are discrete in time, which results in a discontinuous evolution of f_{coll} as well. The resulting $\langle J_\nu \rangle_{\text{LW, homo, discrete}}$ plotted in Figure 8 agrees well with the globally-averaged value of $\langle J_\nu \rangle_{\text{LW, sim}}$ from our simulations, as expected. For comparison, we also plot in Figure 8 the homogeneous approximation result when the discrete, time-stepped collapsed fractions, f_{coll} , shown in Figure 7 are replaced by a smoothly varying mass function based on fitting the N-body results over time. The importance of the H Lyman line opacity in attenuating the LW photons is illustrated by the quantity $\langle J \rangle_{\text{LW, homo, thin}}$, also plotted in Figure 8, the unattenuated mean intensity in the homogeneous approximation if we neglect H Lyman line opacity but take account of the ultimate horizon which corresponds to the distance from which Lyman limit photons at 13.6 eV redshift to the minimum energy (11.5 eV) of interest here for the LW dissociation rate.

Which sources are the dominant contributors to J_ν , sources *near* to or sources *far* from the observer? Let us consider the same homogeneous universe as described above. If photons were not attenuated ($f_{\text{mod}} = 1$), and the comoving emission coefficient $\bar{j}_{\nu_s}(z_s)$ remained constant over time, then spherical shells with identical proper thickness $\Delta \left(\frac{dr_{\text{os}}}{1+z_s} \right)$ would contribute equally to J_ν , as seen in equation (see 29). This is not the case, however. The factor f_{mod} increases as r_{os} decreases (Figure 3), and f_{coll} usually increases as z_s decreases as well. These two factors combine to make nearby sources more important. An opposite trend can occur, however, if we consider only the sources inside low-mass halos, because the evolution of their emission coefficient is not monotonic, as seen in Figure 7. That nonmonotonicity is not enough to completely offset the increase of f_{mod} , however. Defining the fractional contribution from spheres of varying radius r_{os} as

$$f(< r_{\text{os}}) \equiv \int_0^{r_{\text{os}}} \left(\frac{dr_{\text{os}}}{1+z_s} \right) \bar{j}_{\nu_s}(z_s) \cdot f_{\text{mod}}(r_{\text{os}})$$

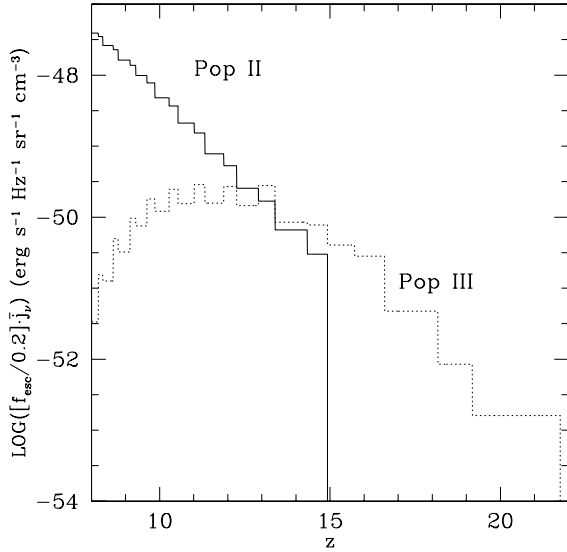


Figure 7. Comoving emission coefficients $\bar{j}_{\nu_s}(z_s)$ from Pop III objects (dotted) residing in low-mass ($10^8 \leq M/M_\odot \leq 10^9$) halos and Pop II objects (solid) residing in high-mass ($M/M_\odot \geq 10^9$) halos. These are constant during the source lifetime $\Delta t \approx 20$ Myrs, because halo collapsed fractions, obtained from the self-regulated simulation results (IMSP), are also assumed to be constant during Δt , which is also identical to the time interval between adjacent N-body outputs.

$$/ \int_0^{r_{\text{LW}}} \left(\frac{dr_{\text{os}}}{1+z_s} \right) \bar{j}_{\nu_s}(z_s) \cdot f_{\text{mod}}(r_{\text{os}}), \quad (30)$$

we have calculated $f(< r_{\text{os}})$ both for low-mass halo sources and high-mass halo sources. The results for the low-mass (suppressible) and high-mass (not suppressible) halos are plotted in Figure 9. In the case of $J_{\text{LW, HM}}$, for example, while all sources within r_{LW} can contribute, $\sim 80\%$ of $J_{\text{LW, HM}}$ is contributed by sources at $r \lesssim [0.35 - 0.45]r_{\text{LW}}$. In the case of $J_{\text{LW, LM}}$, the overall trend is similar to that for $J_{\text{LW, HM}}$, except at $z \simeq 8$. Even at this redshift, however, an observer primarily needs to look back only to $r \simeq 0.4r_{\text{LW}}$, since the high-mass halos dominate the total emissivity at late times, as seen in Figures 7 and 9, and dominate J_{LW} , as well, therefore.

While our comparison of the simulated, globally-averaged LW background with that from the homogeneous approximation shows that the latter is good as long as we give it the correct, self-regulated, space-averaged mass function of source halos, only the *simulations* can tell us about the spatial *variations* in the LW background and their evolution, as well. We will show in the following section that a significant spatial fluctuation of the LW background does arise during the epoch of reionization. This, in principle, could induce a fluctuating feedback effect on the star formation in minihalos, thereby altering the apparent pattern of their clustering from that which arises gravitationally due to structure formation.

Note that the possible effect by the finite size of the box, which is smaller than the LW horizon, does not seem to affect our quantitative conclusion too much. First, as

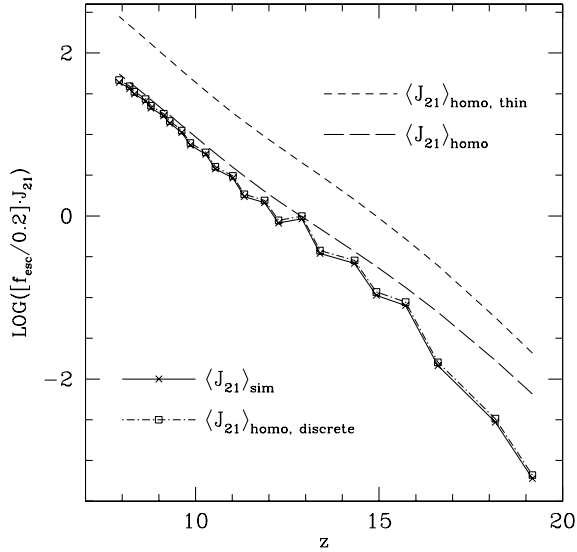


Figure 8. Evolution of the global average LW background intensity (in units of 10^{-21} erg cm $^{-1}$ s $^{-1}$ Hz $^{-1}$ ster $^{-1}$) $\langle J_\nu \rangle_{LW,21}$: $\langle J_\nu \rangle_{LW,21}$ (solid-cross), the intensity obtained by averaging the LW background field over the simulation volume at each redshift z , $\langle J_\nu \rangle_{LW,21,hom}$ (dot-dashed-square), the mean intensity in a homogeneous universe but with the emission coefficient depicted in Figure 7 (i.e. discrete in time). We also plot the average intensity, $\langle J_\nu \rangle_{LW,21,semi}$ (long-dash), based upon our smooth fitting formulae (i.e. continuous in time) for the collapsed fractions of both low-mass ($10^8 \leq M/M_\odot \leq 10^9$) and high-mass ($M/M_\odot \geq 10^9$) halos. For comparison, $\langle J_\nu \rangle_{LW,21,semi,OT}$ (short dash) is the intensity when we neglect the optical depth to H Lyman lines but take the horizon as the distance over which Lyman limit photons (13.6 eV) redshift to the minimum energy (11.5 eV) photons of our interest.

described above, about 80% of the LW intensity comes from $r \lesssim [0.35 - 0.45]r_{LW}$, which is just about the box size used. This implies that the fluctuation of LW intensity as well as its mean is contributed mostly by nearby sources. Second, according to a suite of structure formation simulations we have performed, halo mass functions dn/dM from these simulations do not show too much suppression at a mass scale corresponding to the mass of the box, where most of the suppression of power is expected to occur. Mass functions from these simulations (in varying dynamical ranges), accordingly, connect smoothly when plotted on a single viewgraph. Because LW intensity originates from sources of reionization residing in cosmological halos, power of the LW intensity fluctuation at the box scale would not be suppressed just as the mass function dn/dM at the box scale is not.

3.3. Spatial Fluctuations of the LW background

Until now, the possible spatial fluctuations of the LW background have been neglected, due partly to the fact that r_{LW} is a cosmologically large scale. One might naively have expected, therefore, that the LW intensity fluctuations inside the LW band photon

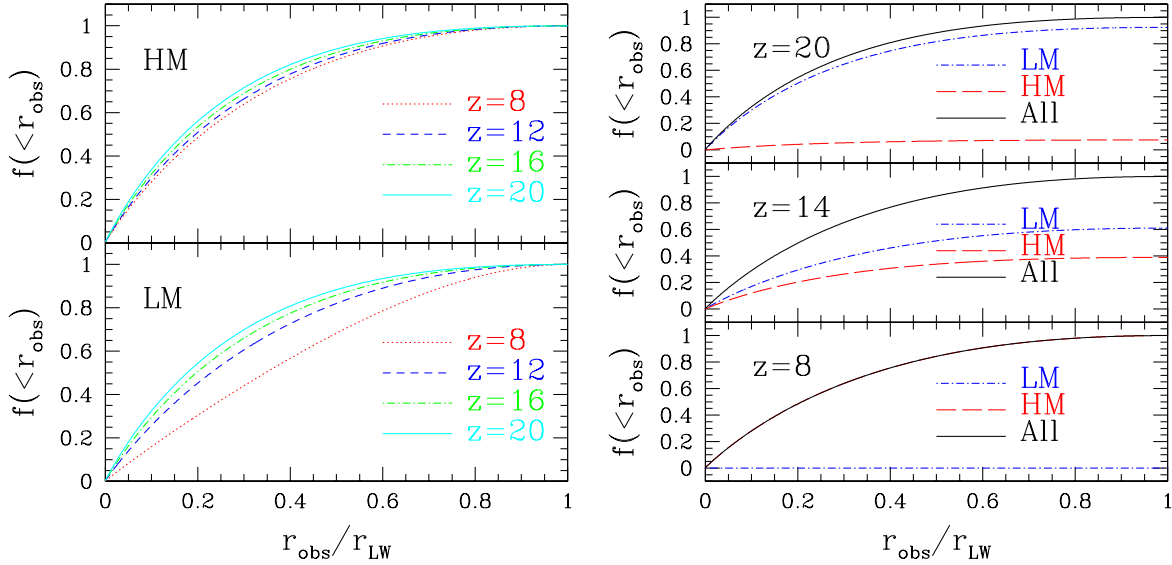


Figure 9. Fractional contribution to J_ν from sources inside a sphere of comoving radius r_{os} (normalized to r_{LW}) from the observer. This is separated into two categories by mass: (*top-left*) contribution to $J_{\text{LW, HM}}$, or the intensity J_{LW} only by sources in high-mass ($M/M_\odot \geq 10^9$) halos. (*bottom-left*) contribution to $J_{\text{LW, LM}}$, or the intensity J_{LW} only by sources in low-mass ($10^8 \leq M/M_\odot \leq 10^9$) halos. (*right*) Fractional contribution to the total J_{LW} by low-mass halo sources (LM, dot-dashed), high-mass halo sources (HM, dashed), and all sources (All, solid). Low-mass halo contribution, dominating J_{LW} at $z \sim 20$, becomes comparable to high-mass halo contribution at $z \sim 14$, and becomes negligible at $z \sim 8$. Considering both (All) contributions, about 80% of J_{LW} comes from $r \lesssim [0.35 - 0.45]r_{\text{LW}}$ at all redshifts. This indicates that both isotropic and fluctuating components of the LW background are dominated by nearby sources at all times.

horizon, or r_{LW} , are negligibly small, since the fluctuations in the space-density of matter are small when averaged on such large scales at such an early epoch. Nevertheless, as we will show, we find huge fluctuations in the LW radiation field. How is this possible? In this section, we present our results for the fluctuations in the LW radiation field and explain their origin.

In Figure 10, we show the $J_{\text{LW}, 21}$ field on a planar slice (with fixed comoving coordinates) inside the simulation box at different redshifts. $J_{\text{LW}, 21}$ varies significantly in space at all redshifts. For instance, at $z = 16.602$, the overall variance of $J_{\text{LW}, 21}$ is about two orders of magnitude. Figure 10 shows that as many as 3 contour levels are observed simultaneously in the same image plane at this redshift, corresponding to $J_{\text{LW}, 21} = 0.01, 0.1, \text{ and } 1$, respectively. This example clearly debunks any previous assumption that might have been made that only small fluctuations would exist in the LW background inside r_{LW} .

The PDF of $J_{\text{LW}, 21}$ values on the simulation grid, plotted in Figure 11, is also noteworthy. The volume-weighted distribution of $J_{\text{LW}, 21}$ is highly skewed. The deviation of $J_{\text{LW}, 21}$ from the global average, $\langle J_{\text{LW}, 21} \rangle$, is small when $J_{\text{LW}, 21} < \langle J_{\text{LW}, 21} \rangle$ (or $\delta_J < 0$,

where $\delta_J \equiv (J - \langle J \rangle) / \langle J \rangle$. The minimum fluctuation is $\delta_{J,\min} \approx -0.5$ at our starting redshift, approaching zero as time goes on. Roughly speaking, $J_{\text{LW},21} \simeq \langle J_{\text{LW},21} \rangle$ when $\delta_J < 0$. In contrast, strong deviations are observed in regions with $\delta_J > 0$. Accordingly, most of the fluctuation involves $J_{\text{LW},21} > \langle J_{\text{LW},21} \rangle$. At all redshifts, $J_{\text{LW},21}$ shows a variation of about two orders of magnitude from the minimum to the maximum, and about an order of magnitude variation at the 99.73% level.

The (sample) variance of $J_{\text{LW},21}$, $\sigma_J^2 \equiv \langle \delta_J^2 \rangle$, also plotted in Figure 11, does not evolve in a monotonic way. It starts out very large at $z \approx 19.2$ and slowly decreases in time until $z \approx 15$, then increases again until $z \approx 12$ (except for a brief, sudden drop at $z \approx 13$), and finally decreases again after $z \approx 12$. This limited range of redshift where σ_J^2 reverses its evolutionary trend, $z \approx [15 - 12]$, corresponds to the epoch when sources start to form inside massive halos with $M \geq 10^9 M_\odot$, which are not subject to suppression and “self-regulation” (see Figure 7). We suspect that the small sudden drop of σ_J^2 at $z \approx 13$, however, is just due to the inherent cosmic variance.

The power spectrum of δ_J , $P(k)$, is shown in Figure 12. Large scales (small k) have more power than small scales (large k) do. The shape of $P(k)$ is rather complex, and a simple power-law provides a poor fit. Nevertheless, if a local power-law fitting is used, its power index becomes steeper in time. The overall amplitude of $P(k)$ decreases in time almost monotonically, except for an increase from $z \approx 15$ to $z \approx 12$, which is consistent with the trend seen in the evolution of σ_J^2 in Figure 11. As for the normalization constant of $P(k)$, we follow the convention that the variance of δ_J is given by

$$\sigma_J^2 \equiv \langle \delta_J^2 \rangle = \frac{1}{2\pi^2} \int_0^\infty P(k) k^2 dk, \quad (31)$$

in the limit in which the size of the volume over which the average is calculated becomes infinitely large.

What causes such huge fluctuations within the simulation box, even when its size is smaller than r_{LW} ? The answer is straightforward: radiation sources cluster on scales smaller than r_{LW} , and their spatial clustering generates fluctuations in the LW background that are not washed out even after the fluxes from all sources within a distance r_{LW} are added up. The original assumption that the LW background would evidence only small fluctuations misses this important ingredient. As simulated and noted by Iliiev, Mellema, Pen, Merz, Shapiro and Alvarez (2006) and others, patchiness of cosmic reionization, itself, strongly reflects the source-clustering effect. Sources cluster in high-density regions and will also produce a stronger LW background nearby, therefore. Such a correlation between the LW fluctuations and the matter density fluctuations is depicted in Figure 13.

Since reionization is “inside-out” according to these simulations (i.e. the high-density regions ionize first), there is also a correlation between the H II regions and the regions of higher-than-average LW intensity, as seen in Figure 10. In fact, an animated sequence of maps like those in Figure 10 shows that isocontours of $J_{\text{LW},21}$ start out centered on the same density peaks where H II regions first appear. However, the isocontours of $J_{\text{LW},21}$ expand more rapidly than the ionization fronts (“I-fronts”) that

define the H II boundaries, overtaking the I-fronts and expanding beyond the H II regions.

Finally, we focus our attention on the LW intensity field in the neutral regions alone. Some fraction of the Pop III stars, including the very first ones, are believed to have formed inside cosmological minihalos. Minihalos in *ionized* regions are less likely to have formed stars, however. If a minihalo formed in the ionized region, “Jeans-mass filtering” would have meant that it formed of dark matter only, devoid of baryons (e.g. Shapiro et al., 1994). On the other hand, if a *pre-existing* minihalo found itself inside an ionized region that had expanded to overtake it before the minihalo had yet formed a star, such a minihalo would have photoevaporated in the ionized region (Shapiro et al., 2004; Iliev et al., 2005). Accordingly, star formation in minihalos in ionized regions was suppressed even more readily and further than in the low-mass atomic-cooling sources, halos with mass $M \geq 10^8$. As far as star formation in minihalos is concerned, therefore, the *neutral* regions of the IGM are of particular interest. We find (see Figure 14) that early-on, the PDF distribution of $J_{\text{LW},21}$ in the neutral regions is very similar to that overall, except with the highest-flux tail of the distribution cut off, since those are the regions in the immediate vicinity of the ionizing sources, which are ionized first. The standard deviation of the PDF of $J_{\text{LW},21}$ decreases in time more rapidly for the neutral regions than for that overall. During the late stages of reionization, the values of $J_{\text{LW},21}$ in these neutral cells converge to the average value, $\langle J_{\text{LW},21} \rangle$, and the fluctuations largely disappear.

4. Conclusion and Future Prospects

We have, for the first time, calculated the inhomogeneous background of H₂ dissociating UV radiation caused by the same sources which reionized the Universe in a large-scale radiative transfer simulation of cosmic reionization. The UV continuum emitted below 13.6 eV by each source was transferred through the IGM, attenuated by atomic H Lyman series resonance lines, to predict the evolution of the inhomogeneous radiation background in the energy range of the LW band of H₂ between 11 and 13.6 eV. This required us to transfer the radiation from the many thousands of source galactic halos in our simulation, which resolved all halos of mass above $10^8 M_\odot$ in a comoving volume of $(50 \text{ Mpc})^3$, from each source to each of the millions of grid cells of our reionization simulation. To accomplish this, we developed a novel method to calculate the attenuation of LW band photons from individual sources by H Lyman series resonance lines, an otherwise prohibitively expensive, multi-frequency calculation, in a very fast way, instead, without an explicit multi-frequency operation. This was achieved by a grey opacity approximation, the “picket-fence” modulation factor, a simple function of the comoving distance between a source and an observer, which represents the frequency-averaged attenuation of LW band photons. We also explicitly accounted for the effect of the finite light-crossing time between sources and observers, by constructing the conformal space-time diagram of all reionization sources and observer grid cells and

finding the intersections between source world lines and observer past light cones.

Our results here demonstrate that the rise of the cosmic LW background to levels which have previously been identified as the threshold for dissociating H₂ and thereby suppressing star formation inside minihalos occurs well before the epoch of reionization is very advanced. Not only is this the case for the mean LW background intensity, as anticipated by earlier estimates based upon a homogeneous universe approximation, but it is even more the case for the inhomogeneous background. The first regions to form halos are the regions with the highest mean overdensity, and we show that this is where the LW background rises the fastest and is at the highest levels. This means that our assumption here, for simplicity, that reionization is dominated by the atomic cooling halos, and that minihalos are sterilized by the rising LW background before they can contribute significantly to the ionizing and, accordingly, the LW background, as well, is self-consistent.

On the other hand, since there are also some minihalos that form far from the density peaks around which the halos cluster, we might also expect that there are *some* minihalos that form far from the peaks in the LW background, before their local LW intensity has risen to the threshold level for H₂ suppression. In the future, it will be interesting to consider the possible role of these minihalos that form in places where the LW background is not high enough to suppress their star formation.

Our result can be used for various applications. For example, fluctuating H₂ abundance in IGM and cosmological halos may be calculated inside our simulation box. This would at least require implementing reaction rates of neutral and ionic species of H, He, and H₂. One may have to run many small-box simulations similar to those of Yoshida et al. (2003), in order to calculate H₂ abundance and track source formation inside cosmological halos under fluctuating J_{LW} calculated in this paper. Similarly, once X-ray emitting sources are properly populated in the simulation box, a composite effect of negative (due to photodissociation by UV) and positive (due to partial ionization by X-ray) feedback may be studied as well.

There is the possibility that source formation inside the more massive, atomic-cooling halos is affected by the LW background, too, because molecular cooling takes place inside these halos in the following way. When the gas cools from the ionized state in these halos, it does so out of equilibrium (e.g. Shapiro and Kang 1987; Kang and Shapiro 1992): gas cools faster than it recombines, so even after atomic H cooling has reached its typical saturated phase at $T \lesssim 10^4$ K, there still remains a significant trace amount of electrons. Gas-phase reactions can then create H₂ with the help of these electrons, which can further cool the gas down to $T \sim 200$ K. Even though H₂ at this stage can become self-shielded against the UV dissociating background (Oh and Haiman 2002), a strong enough background may nevertheless dissociate H₂ and suppress star formation to some extent (HAR). The threshold LW intensity for such suppression inside these atomic cooling halos, $(J_{\text{LW}})_{\text{threshold,atomic}}$, is believed to be much larger than $(J_{\text{LW}})_{\text{threshold}}$ for minihalos (HAR). This might, therefore, somewhat affect the history of cosmic reionization near the end of reionization,

when even $(J_{\text{LW}})_{\text{threshold,atomic}}$ has been reached.

Emissivity by the first stars that contribute to the cosmic near-infrared background (NIRB) may also be affected by the fluctuating LW background calculated here. Observations of a strong NIRB excess over the known foreground have been reported (e.g. Matsumoto et al. 2005), and this has been interpreted as a possible signature of the first stars (c.f. Madau 2006 and references therein), although the true identity of the contributing sources is currently under debate (e.g. Kashlinsky et al. 2007; Thompson et al. 2007). Our work will impact the interpretation of both the homogeneous and inhomogeneous components of the NIRB, because predictions of the first star formation should be strongly affected by our results.

We argued in § 2 that we are justified in neglecting H₂ self-shielding by the IGM in calculating the opacity to LW photons. This was justified by the fact that the concentration of H₂ in the pre-reionization IGM was only $\sim 10^{-6}$ and, as such, $\tau_{\text{H}_2} \lesssim 1$. However, we can now use hindsight to see that our neglect of τ_{H_2} is even more self-consistent than that estimate would suggest. Hydrogen molecules in the IGM are quickly dissociated by the rising LW background. It is easily seen from Figures 6, 10 and 11 that $J_{\text{LW},21} \gtrsim 10^{-2}$ at $z \simeq 20$ in the vicinity of atomic cooling halos, and the mean value quickly rises to $\langle J_{\text{LW},21} \rangle \simeq 10^{-2}$ and above. When the mean IGM prior to reionization (with temperature $T_{\text{IGM}} \simeq 369(1+z)^2/135^2$, hydrogen number density $n_{\text{H}} \simeq 1.7 \times 10^{-3} (1+z)^3/21^2 \text{ cm}^{-3}$, and $y_{\text{H}_2} \simeq 2 \times 10^{-6}$ when there is no LW background) is exposed to the LW intensity $J_{\text{LW},21} = 10^{-2}$ from $z = 20$ onward, for example, its molecular fraction drops to $y_{\text{H}_2} \simeq 2 \times 10^{-7}$ by $z \simeq 17$. Even if H₂ self-shielding were marginally important with $y_{\text{H}_2} \simeq 2 \times 10^{-6}$ at high redshift (Ricotti et al. 2002), therefore, this will quickly become negligible when molecules are dissociated to the level $y_{\text{H}_2} \simeq 2 \times 10^{-7}$, which would occur at $z \simeq 17$ from the LW background contributed by the atomic-cooling halos alone. Peculiar motion of gas elements will weaken self-shielding even further (e.g. Machacek et al. 2001). Johnson et al. (2007), on the other hand, claim that relic H II regions created by the first stars can recombine and generate abundant H₂ before being exposed to other external sources, through the nonequilibrium H₂-formation mechanism described above (Shapiro and Kang 1987; Kang and Shapiro 1992). Johnson et al. (2007) find, however, that this boost of H₂ abundance is delayed significantly when $J_{\text{LW},21} \gtrsim 10^{-2}$, which is easily satisfied in the mean IGM at $z \simeq 17$ and in the vicinity of atomic cooling halos at $z \simeq 20$. This suggests that the proposed nonequilibrium enhancement of the H₂ concentration in the IGM inside relic H II regions is not likely to provide a significant enough H₂ opacity to shield the IGM through most of the EOR.

Acknowledgments

This study was supported in part by KICOS through the grant K20702020016-07E0200-01610 provided by MOST, NSF grant AST 0708176, NASA grants NNX07AH09G and NNG04G177G, Chandra grant SAO TM8-9009X, Swiss National Science Foundation

grant 200021-116696/1, and Swedish Research Council grant 60336701. The authors acknowledge the Texas Advanced Computing Center (TACC) at The University of Texas at Austin for providing HPC resources that have contributed to the research results reported in this paper.

References

- Abgrall H and Roueff E 1989 *Astron. Astrophys. Suppl. Ser.* **79**, 313–328.
- Ahn K and Shapiro P R 2007 *Mon. Not. R. Astron. Soc.* **375**, 881–908.
- Ahn K, Shapiro P R, Iliev I T, Mellema G and Pen U L 2008 *in* ‘First Stars III’ Vol. 990 of *American Institute of Physics Conference Series* pp. 374–376.
- Alvarez M A, Bromm V and Shapiro P R 2006 *Astrophys. J.* **639**, 621–632.
- Barkana R and Loeb A 2005 *Astrophys. J.* **626**, 1–11.
- Bromm V, Kudritzki R P and Loeb A 2001 *Astrophys. J.* **552**, 464–472.
- Bromm V and Larson R B 2004 *Ann. Rev. Astron. Astrophys.* **42**, 79–118.
- Gnedin N Y and Hui L 1998 *Mon. Not. R. Astron. Soc.* **296**, 44–55.
- Haiman Z, Abel T and Rees M J 2000 *Astrophys. J.* **534**, 11–24.
- Haiman Z and Bryan G L 2006 *Astrophys. J.* **650**, 7–11.
- Haiman Z, Rees M J and Loeb A 1997 *Astrophys. J.* **484**, 985–+.
- Höhne F E and Zimmermann R 1982 *J. Phys. B: At. Mol. Phys.* **15**, 2551–2561–851.
- Iliev I T, Ciardi B, Alvarez M A, Maselli A, Ferrara A, Gnedin N Y, Mellema G, Nakamoto T, Norman M L, Razoumov A O, Rijkhorst E J, Ritzerveld J, Shapiro P R, Susa H, Umemura M and Whalen D J 2006 *Mon. Not. R. Astron. Soc.* **371**, 1057–1086.
- Iliev I T, Mellema G, Pen U L, Merz H, Shapiro P R and Alvarez M A 2006 *Mon. Not. R. Astron. Soc.* **369**, 1625–1638.
- Iliev I T, Mellema G, Shapiro P R and Pen U L 2007 *Mon. Not. R. Astron. Soc.* **376**, 534–548.
- Iliev I T, Shapiro P R, McDonald P, Mellema G and Pen U L 2007 *submitted to Mon. Not. R. Astron. Soc.* , *ArXiv e-prints (0711.2944)* .
- Iliev I T, Shapiro P R and Raga A C 2005 *Mon. Not. R. Astron. Soc.* **361**, 405–414.
- Johnson J L, Greif T H and Bromm V 2007 *Astrophys. J.* **665**, 85–95.
- Kang H and Shapiro P R 1992 *Astrophys. J.* **386**, 432–451.
- Kashlinsky A, Arendt R G, Mather J and Moseley S H 2007 *Astrophys. J. Lett.* **666**, L1–L4.
- Machacek M E, Bryan G L and Abel T 2001 *Astrophys. J.* **548**, 509–521.
- Madau P 2006 *Nature* **440**, 1002–1003.

- Matsumoto T, Matsuura S, Murakami H, Tanaka M, Freund M, Lim M, Cohen M, Kawada M and Noda M 2005 *Astrophys. J.* **626**, 31–43.
- Mellema G, Iliiev I T, Alvarez M A and Shapiro P R 2006 *New Astronomy* **11**, 374–395.
- Merz H, Pen U L and Trac H 2005 *New Astronomy* **10**, 393–407.
- Mesinger A, Bryan G L and Haiman Z 2006 *Astrophys. J.* **648**, 835–851.
- Mesinger A and Dijkstra M 2008 *ArXiv e-prints (0806.3090)* .
- Oh S P and Haiman Z 2002 *Astrophys. J.* **569**, 558–572.
- Oh S P and Haiman Z 2003 *Mon. Not. R. Astron. Soc.* **346**, 456–472.
- O’Shea B W and Norman M L 2008 *Astrophys. J.* **673**, 14–33.
- Pritchard J R and Furlanetto S R 2006 *Mon. Not. R. Astron. Soc.* **367**, 1057–1066.
- Ricotti M, Gnedin N Y and Shull J M 2002 *Astrophys. J.* **575**, 49–67.
- Shapiro P R, Giroux M L and Babul A 1994 *Astrophys. J.* **427**, 25–50.
- Shapiro P R, Iliiev I T and Raga A C 2004 *Mon. Not. R. Astron. Soc.* **348**, 753–782.
- Shapiro P R and Kang H 1987 *Astrophys. J.* **318**, 32–65.
- Susa H and Umemura M 2006 *Astrophys. J. Lett.* **645**, L93–L96.
- Thompson R I, Eisenstein D, Fan X, Rieke M and Kennicutt R C 2007 *Astrophys. J.* **666**, 658–662.
- Tumlinson J and Shull J M 2000 *Astrophys. J. Lett.* **528**, L65–L68.
- Wise J H and Abel T 2007 *Astrophys. J.* **671**, 1559–1567.
- Yoshida N, Abel T, Hernquist L and Sugiyama N 2003 *Astrophys. J.* **592**, 645–663.
- Yoshida N, Oh S P, Kitayama T and Hernquist L 2007 *Astrophys. J.* **663**, 687–707.

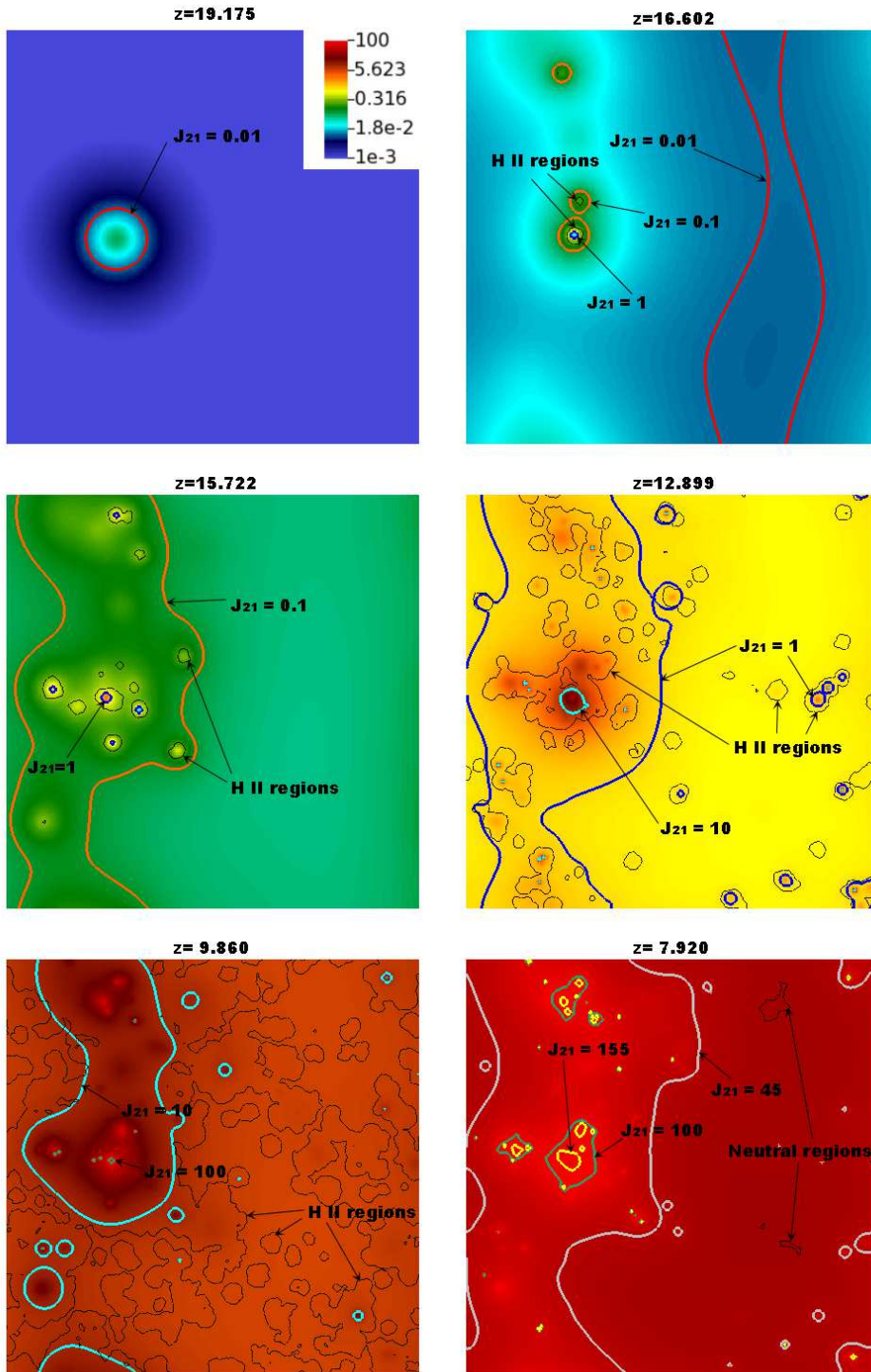


Figure 10. Simulation spatial images showing the isocontours of patchy reionization and the patchy H_2 dissociating background on a planar slice through the box of volume $(35 h^{-1} \text{cMpc})^3$ at different epochs. The level of $J_{\text{LW},21}$ on the grid is depicted by different colors, with the range $[10^{-3} - 10^2]$, shown on the inset of the top-left panel. On top of each $J_{\text{LW},21}$ color-map, contours of thick colored lines represent different $J_{\text{LW},21}$ levels (red, orange, blue, cyan, and green corresponding to $J_{\text{LW},21} = 0.01, 0.1, 1, 10, \text{ and } 100$, respectively). The black lines represent the ionization fronts characterized by $x = 0.5$.

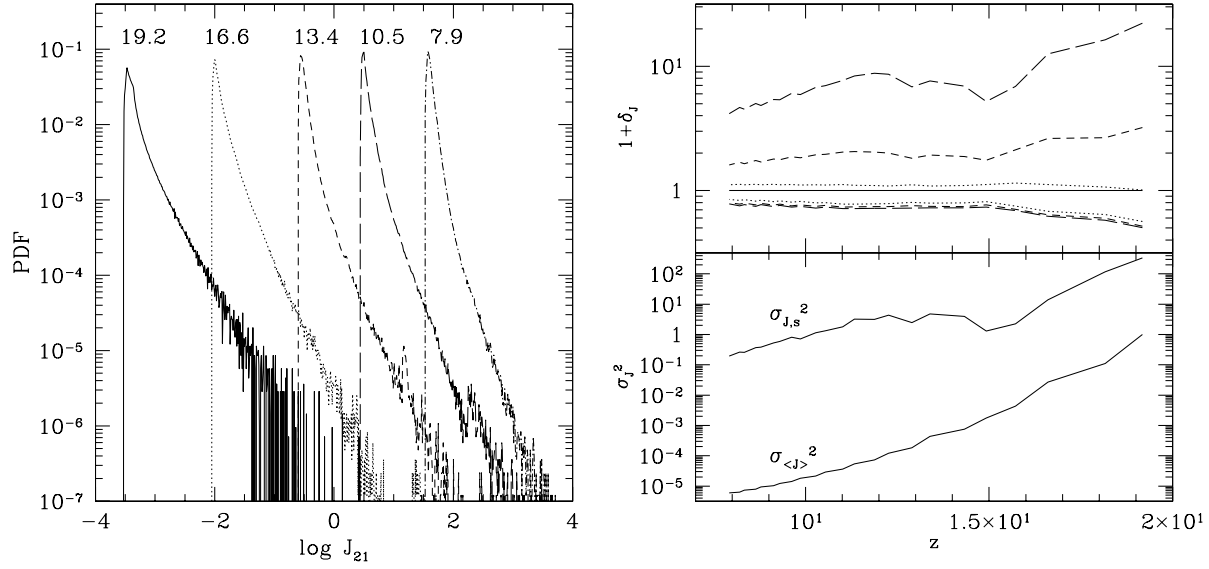


Figure 11. (*left*) Probability distribution function (“PDF”) of $J_{\text{LW},21}$ for the 203^3 grid cells inside a box of comoving size $35 h^{-1}$ Mpc at different redshifts. Numbers on individual curves represent the corresponding redshifts. (*right*) The top panel shows deviation of $J_{\text{LW},21}$ from the globally-averaged $\langle J_{\text{LW},21} \rangle$, expressed in terms of $1 + \delta_J$. Around the curve of $\langle J_{\text{LW},21} \rangle$ (solid), contours containing 68.27% (dotted), 95.45% (short dashed), and 99.73% (long dashed) of the $J_{\text{LW},21}$ distribution are shown. The sample variance of $J_{\text{LW},21}$, $\sigma_{J,s}^2$, is plotted together with the variance on the average, $\sigma_{\langle J \rangle}^2$, in the bottom panel. $\sigma_{\langle J \rangle}^2$ is dominated by the Poisson error from the number of radiation sources rather than the number of simulation grids, because the former is found to be much smaller than the latter at all redshifts of our interest in our simulation box.

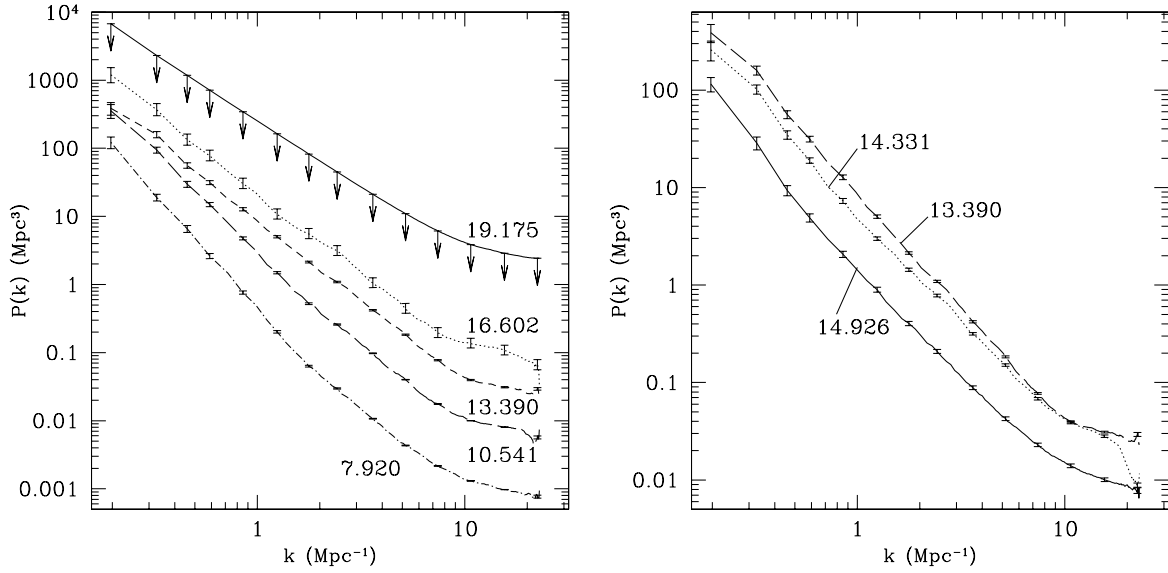


Figure 12. (*left*) Power spectrum $P(k)$ of LW background fluctuations δ_J at different redshifts. Numbers next to plotted curves represent corresponding redshifts. (*right*) $P(k)$ at limited range of redshifts, $z \approx 15 - 13.4$. These show a reversed evolutionary track, increasing in time, compared to $P(k)$'s plotted on the left panel, decreasing in time. Note that this trend can also be seen in Figure 11. Error bars on both plots represent variance of $P(k)$ due to the finite number of wavenumbers and the finite number of radiation sources. At $z = 19.175$, there is only one radiation source in the box, and the corresponding power spectrum is roughly identical to the upper limit of $P(k)$.

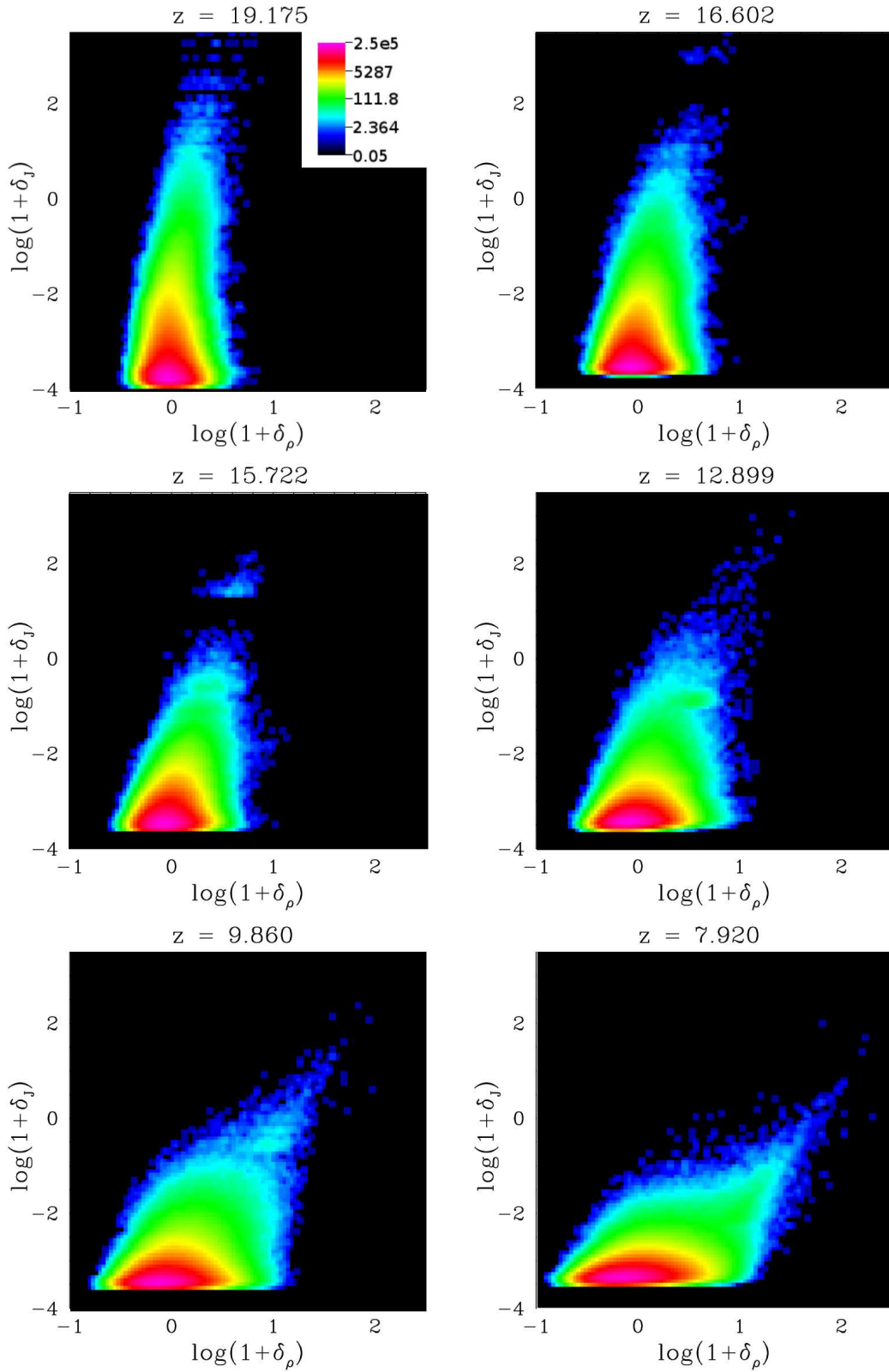


Figure 13. Correlation of $J_{\text{LW},21}$ and ρ_m at different epochs, depicted by the number of cells at given δ_J and δ_{ρ_m} , with uniform bin-size of $\log(1+\delta_\rho)$ and $\log(1+\delta_J)$. Redshifts of these panels match those of Fig 10. The inset in the top left panel shows the color scheme to depict the number of grid cells.

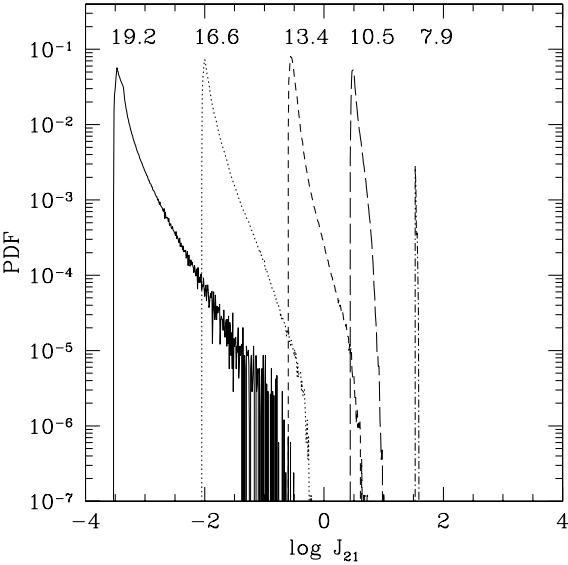


Figure 14. Probability distribution of $J_{LW,21}$ in neutral cells only. Compare this plot to Fig 11. Decrease of overall area of PDF in time simply reflects the fact that the total volume of neutral regions decreases as cosmic reionization proceeds.